Remote Sensing of Environment 331 (2025) 115023

Contents lists available at ScienceDirect

Remote Sensing of Environment

journal homepage: www.elsevier.com/locate/rse

Geodetic glacier mass balance in the Karakoram (2011–2019) from TanDEM-X: An InSAR DEM differencing framework

Shiyi Li [a,*], Irena Hajnsek [a,b]

[a] Institute of Environmental Engineering, ETH Zürich, Zürich, 8093, Switzerland
[b] Microwaves and Radar Institute, German Aerospace Centre (DLR) e.V., Wessling, 82234, Germany

ARTICLE INFO

Edited by Menghua Wang

Keywords:
Karakoram
Glacier
Elevation change
Mass balance
TanDEM-X
InSAR

ABSTRACT

Glaciers serve as sensitive indicators of climate change, influencing both regional water supplies and global sea-level rise. Contrasting to the global tendency towards retreat, glaciers in the Karakoram exhibits an unusual pattern of stability and modest thickening. However, the spatial variability and underlying causes of the mass balance anomalies remain insufficiently understood, primarily due to the limitations in previous measurement methods. To address this gap, we conducted a comprehensive geodetic analysis of glacier elevation changes in the central and eastern Karakoram, covering 681 glaciers of over 10,000 km^2 between 2011 and 2019. The elevation was measured exclusively with TanDEM-X InSAR data to reduce penetration bias and temporal ambiguities. The geodetic analysis was conducted using a three-module DEM Differencing framework. In this framework, the first module generates high-quality InSAR DEM with an iterative approach to address the challenges of mountainous terrain for InSAR processing; the second module employed an innovative voids filling method using Gaussian Process Regression for robust elevation change mapping; and the third module incorporates a non-stationary uncertainty analysis for rigorous uncertainty quantification. The results reveal a regional mean elevation change rate of $0.0038 \pm 0.0042\ \mathrm{m\ yr}^{-1}$ and a specific mass balance of $0.0032 \pm 0.0052\ \mathrm{m\ w.e.\ yr}^{-1}$, indicating slight overall thickening during the study period. The spatial patterns of elevation change display pronounced heterogeneity and clear differences between surge-type and non-surge glaciers, reflecting the complex interplay of dynamic, climatic, and morphological factors in the region. This study demonstrates the capability of high-resolution TanDME-X InSAR DEM for accurate geodetic mass balance analysis in challenging mountain environments. The proposed framework provides a scalable methodology for future large-scale glacier studies.

1. Introduction

Glaciers are vital components of the Earth's cryosphere, playing a key role in regional hydrology and serving as sensitive indicators of climate change (IPCC, 2022). The glacier mass balance reflects the difference between ice accumulation and ablation, offering crucial insights for understanding glacier dynamics and their response to climatic variability (Zemp et al., 2013; Farinotti, 2013; Liu et al., 2021; Bolibar et al., 2022). Studying the mass balance also plays an essential role for assessing a broader environmental processes such as water resource availability, ecosystem functioning, and the impacts of climate change on vulnerable mountain communities (Hirabayashi et al., 2010; Radić and Hock, 2014; Huss and Hock, 2018; Hugonnet et al., 2021; Nie et al., 2021; Zemp et al., 2025).

Recent studies have documented a consistent trend of global glacier mass loss and ice thinning over the past few decades. For instance, Hugonnet et al. (2021) reported a global glacier mass loss of $267 \pm 16\ \mathrm{Gt\ yr}^{-1}$ during 2000–2019, contributing to approximately 21 ± 3 percent of observed sea-level rise. Similarly, Dussaillant et al. (2024) estimated an annual loss of 172 ± 27 Gt equivalent water since 1976, resulting in 22.7 ± 2.3 mm of sea-level rise. More recently, Zemp et al. (2025) reported an average annual glacier mass loss rate of $-273 \pm 16\ \mathrm{Gt\ yr}^{-1}$ during 2000–2023. These findings underscore the critical role of glaciers in driving sea-level rise and highlighted the urgency of understanding regional variations in glacier behavior.

While most glaciers worldwide exhibit a general thinning trend, significant spatial variations and regional heterogeneity exist. One notable exception is the Karakoram region, part of the greater Himalaya–Karakoram–Hindukush (HKH) mountain system. The Karakoram region hosts one of the largest glaciated areas outside the polar regions, estimated from 36,845 km^2 to 50,750 km^2 (Azam et al., 2018). This region

---

* Corresponding author.
E-mail address: shiyi.li@ifu.baug.ethz.ch (S. Li).

https://doi.org/10.1016/j.rse.2025.115023
Received 7 April 2025; Received in revised form 6 September 2025; Accepted 8 September 2025

is of particular importance due to its role in sustaining regional water resources and its unique climatic setting at the confluence of the westerlies and monsoon systems (Mukhopadhyay and Khan, 2014). Since 1997–2001, a phenomenon known as the "Karakoram anomaly" has been observed, where many glaciers remain stable or even gain mass, contrary to the widespread retreat seen in other glacier regions (Hewitt, 2005). This anomaly is believed to result from a combination of various factors, including regional climate variability, the influence of the westerlies, and the insulating effect of debris cover (Farinotti et al., 2020; Dimri, 2021; Lhakpa et al., 2022). Understanding the Karakoram anomaly is crucial for deciphering the complex interplay between climate, glacier dynamics, and regional hydrology.

To enhance the understanding about Karakoram glaciers, large-scale digital elevation models (DEMs) have been widely used to quantify the unique mass balance dynamics in the region. Previous studies have employed DEM derived using either Synthetic Aperture Radar (SAR) or optical stereo images to measure the geodetic mass balance. For instance, Gardelle et al. (2012) measured positive mass balance of $+0.11 \pm 0.22$ m yr^{-1} for 5616 km^2 glaciated area in the central Karakoram during 1999–2008 using DEM obtained from the Shuttle Radar Topography Mission (SRTM) and stereoscopic SPOT-5 imagery. Seasonal difference in the elevation change trends were identified using ICESat time series from 2003 to 2008/09, including positive trends ($+0.41 \pm 0.04$ m yr^{-1}) in winter and slightly negative trends (-0.07 ± 0.04 m yr^{-1}) in autumn (Kääb et al., 2012). Similarly, Rankl and Braun (2016) analyzed 71 glaciers in the central Karakoram (2000–2012) using high-quality DEMs from the TanDEM-X Mission, finding significant distinctions in mass changes for surge (-0.15 ± 0.10 m w.e.yr^{-1}) and non-surge (-0.07 ± 0.10 m w.e.yr^{-1}) glaciers. More recent studies using optical stereo DEMs (2000–2016) have measured GMB of -0.03 ± 0.07 m w.e.yr^{-1} for the region and confirmed that the Karakoram anomaly extends to the western Kunlun and eastern Pamir regions (Brun et al., 2017), with updated analysis showing positive ($+0.12 \pm 0.14$ m w.e.yr^{-1}) and negative (-0.24 ± 0.11 m w.e.yr^{-1}) mass balance for the central and Eastern Karakoram in 2008–2016, respectively (Berthier and Brun, 2019).

Despite these valuable contributions, there remains limitations in current methodologies to obtain accurate and contemporary elevation change measurements in Karakoram. Comparing to optical stereo DEMs, generating DEM with the Interferometric SAR (InSAR) technique has the advantage of having higher spatial resolution and vertical accuracy. However, current InSAR based DEM often relies on SRTM data acquired in 2000 and TanDEM-X DEMs collected between 2011 and 2013. Such restricted temporal span has greatly limited the contemporary assessments of glacier dynamics with InSAR DEM. Integrating optical stereo DEM with InSAR DEM can alleviate such limitation, but the discrepancy in the penetration of the two types of sensors may introduce extra systematic bias and uncertainties (Millan et al., 2015; Dehecq et al., 2016).

To address these limitations and produce high-resolution, contemporary measurements of glacier elevation changes using InSAR data, we exploited TanDEM-X InSAR dataset acquired during its two global missions, including the first mission in 2011–2013 and the second mission in 2017–2020 (Hajnsek et al., 2025). By exclusively using InSAR DEM of the same sensor, we can avoid the penetration bias that is often introduced when combining TanDEM-X with SRTM or optical DEMs (Leinss and Bernhard, 2021; Piermattei et al., 2024). In our work, the InSAR DEM were generated by the raw acquisitions from TanDEM-X individually, which preserved the timestamp of each acquisition and reduced temporal ambiguities. However, using exclusive InSAR data for regional elevation change mapping introduces new challenges for spatial coverage, as the complex terrain of the Karakoram causes large voids in the InSAR DEM due to shadowing, layover, and low coherence. To address this challenge, we developed a Gaussian Process Regression (GPR) method for void filling, enabling robust preservation of the spatial patterns while reconstructing the missing data. We further implemented an uncertainty propagation framework to account for the non-stationarity and spatial correlations of uncertainties.

Through these efforts, we seek to present the recent patterns of elevation and mass change in the Karakoram region during the 2011–2019 period by leveraging the advanced capabilities of the TanDEM-X mission. This can contribute to a better understanding of the Karakoram anomaly and its implications for regional hydrology and climate systems. Additionally, our methodological improvements in DEM generation and void filling can serve as a valuable reference for future studies of glacier mass balance in complex mountain environments.

2. Study region and dataset

2.1. Study region

The specific study region lies within 34.10 °N to 36.53 °N and 74.25 °E to 78.95 °E, covering the central and eastern Karakoram range (Fig. 1). The altitude of the region ranges from about 1000 to more than 8500 m above sea level (m a.s.l.), with a mean altitude of 4580 m a.s.l. The climatic regime is primarily influenced by the mid-latitude westerlies, with a secondary contribution from the South Asian monsoon (Thapa and Muhammad, 2020). The westerlies dominate during the winter and spring, delivering the majority of the annual snowfall, while the monsoon provides limited precipitation during the summer. Pronounced seasonal temperature variations drive surface melt during summer and snow accumulation during winter (Kapnick et al., 2014).

Glaciers in this region span a wide range of elevations, from approximately 3000 to over 7500 m a.s.l., with 60 to 80% of the glaciated area located between 3800 and 5800 m a.s.l. Hewitt (2014). The Karakoram is notable for its distinct glacier dynamics, including frequent surge events characterized by episodic, rapid advances of glacier fronts (Hewitt, 2014; Quincey et al., 2011, 2015). Debris-covered glaciers are also widespread in the region and exhibit lower mass loss rates compared to clean-ice glaciers due to the insulating effect of debris layers (Miles et al., 2018). The interplay of debris cover, steep topographic gradients, and surge dynamics contributes to the spatial heterogeneity of glacier mass balance across the region.

2.2. TanDEM-X data

The TanDEM-X mission, launched by the German Aerospace Center (DLR) in June 2010, was designed to generate a consistent global DEM with unprecedented accuracy using an innovative bi-static satellite formation (Zink et al., 2014; Krieger et al., 2013). The mission's SAR instrument operates in the X-band frequency (9.65 GHz), offering less ground penetration compared to C-band instruments such as SRTM. The initial global DEM acquisition was completed between 2011 and 2014. Building on the mission's stable performance, a new global mission — later referred to as the DEM 2020 mission — was conducted between 2017 and 2020, facilitating the measurement of surface changes on Earth between the two global missions (Lachaise et al., 2020; Hajnsek et al., 2025).

In both mission phases, the TanDEM-X SAR satellites collected Co-registered Single-look Slant-range Complex (CoSSC) data products for DEM generation. Each CoSSC product consists of two focused and co-registered Single Look Complex (SLC) images acquired by the twin satellites operating in bi-static InSAR strip-map mode. With InSAR processing, high-resolution DEMs can be produced from the CoSSC datasets. Each SLC image has a spatial resolution of approximately 3×3 m in both ground range and azimuth, allowing the generation of DEMs with a spatial resolution of approximately 8×8 m.

In this study, we leveraged the raw CoSSC datasets and generated high-resolution DEMs using the proposed InSAR processing pipeline. This approach preserved the acquisition timestamp of each DEM, thereby reducing temporal ambiguity when performing DEM differencing. To minimize seasonal effects in the mass balance calculations,

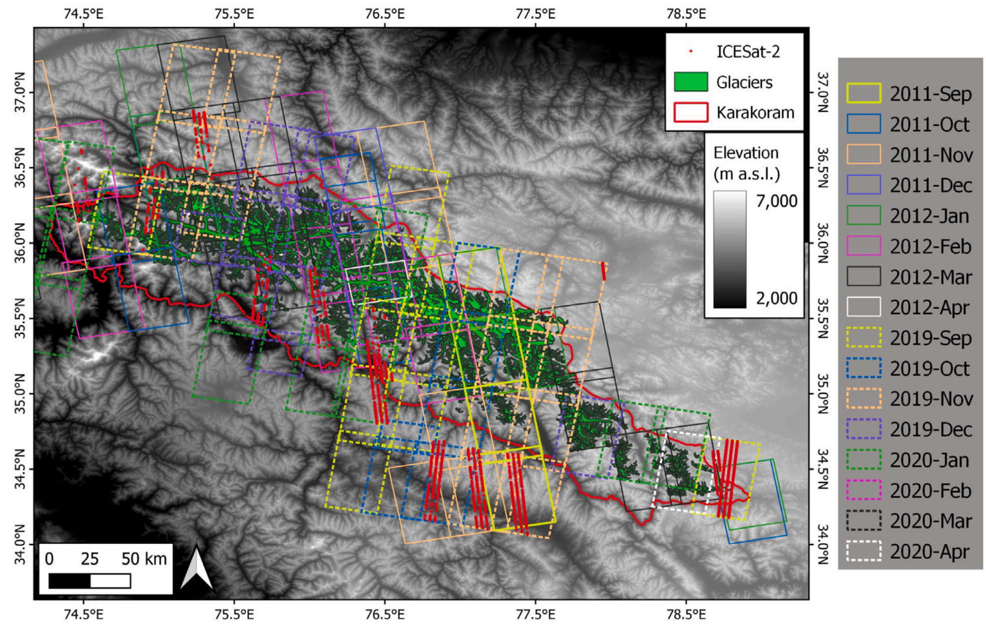

Fig. 1. Overview of the study region and datasets. The Karakoram region is outlined in red, representing the study area. The footprints of individual TanDEM-X acquisitions are displayed as with color-coded rectangles. Glacier outlines (green) are sourced from the Randolph Glacier Inventory (RGI) v7.0 database (RGI Consortium, 2023). ICESat −2 measurements are represented by red dots. The background grayscale shading indicates elevation measured by the Copernicus Global 1-arc-second (COP-30) DEM. (For interpretation of the references to color in this figure legend, the reader is referred to the web version of this article.)

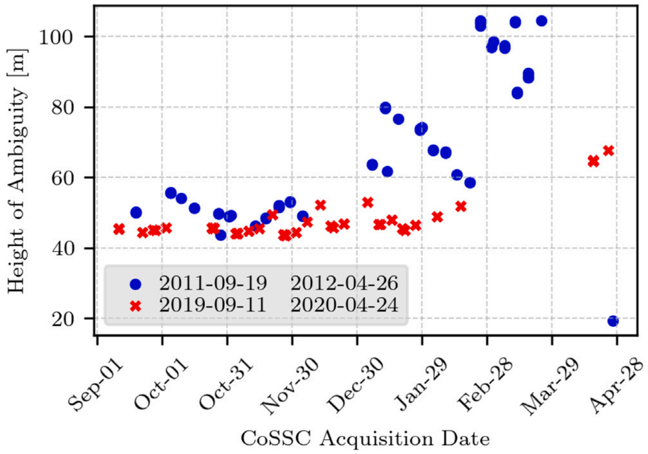

Fig. 2. Height of ambiguity (HOA) of CoSSC products used in this study for 2011 winter (blue dots) and 2019 winter (red cross). (For interpretation of the references to color in this figure legend, the reader is referred to the web version of this article.)

only acquisitions during the accumulation period of a hydrological year (September to April) were used. Specifically, a total of 117 CoSSC images were collected for the Karakoram region, comprising 62 images acquired in 2011–2012 and 55 images in 2019–2020. The 2011 acquisitions were captured exclusively in ascending orbits, while the 2019 acquisitions were captured in descending orbits. The Height-of-Ambiguity (HOA) values ranged from 50 to 100 m for the 2011 images and were consistently around 50 m for the 2019 images (Fig. 2). The nine-year temporal gap between the two datasets satisfies the minimum five-year duration required for applying the constant volume-to-mass conversion factor (Huss, 2013).

2.3. Reference DEM

In this study, the Copernicus Global 1-arc-second (COP-30) DEM was used as the reference in the DEM generation module. Released by the European Space Agency (ESA) in 2020, the COP-30 DEM was derived from the initial global acquisitions of the TanDEM-X mission and provides a vertical Root Mean Square Error (RMSE) of 1.68 m over flat terrain.

Beyond its exceptional vertical accuracy, the COP-30 DEM offers significant advantages when generating DEMs from TanDEM-X CoSSC data. Since it was produced using the same X-band TanDEM-X data, the penetration bias between the reference DEM and the CoSSC measurements is negligible. This eliminates the need for complex corrections related to penetration depth differences, allowing direct updates to the reference DEM through interferometric phase differences to produce the final DEM products.

The COP-30 DEM is referenced in geographic coordinates based on the World Geodetic System 1984 (WGS84), with vertical heights aligned to the EGM2008 geoid model. The dataset covering the study area was obtained through the Copernicus Space Component Data Access PANDA Catalog (European Space Agency and Airbus, 2022).

2.4. Glacier outlines

The glacier outlines used in this study were sourced from the Randolph Glacier Inventory (RGI) v7.0 (RGI Consortium, 2023). Released in September 2023, the RGI v7.0 provides a comprehensive global dataset of glacier outlines, primarily representing conditions around the year 2000.

For the Karakoram region, the inventory includes 17,559 glaciers, covering a total area of 21,675 km^2. To improve the reliability of our analysis, we excluded smaller glaciers with an area less than 0.5 km^2, as they are more prone to higher relative uncertainties in area measurements and contribute minimally to the overall glacier volume. Following this filtering, the final glacier inventory used for mass balance analysis consisted of 4299 glaciers, encompassing a total area of approximately 20,000 km^2.

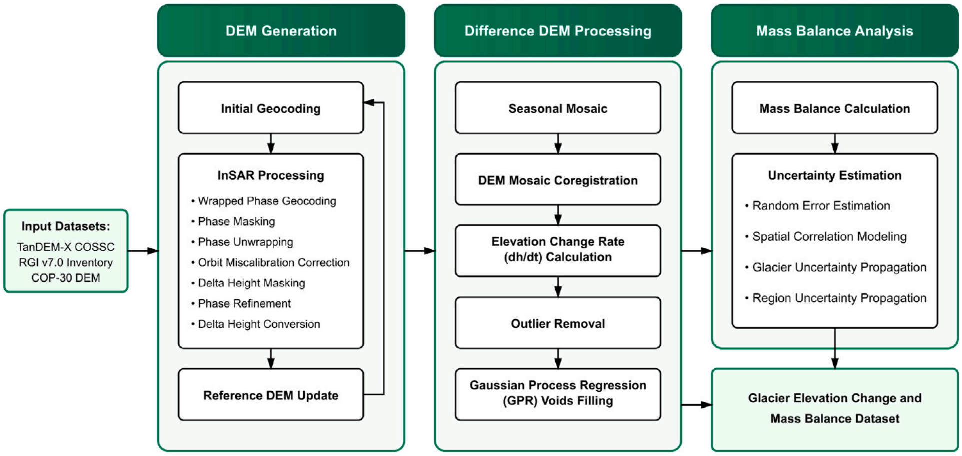

Fig. 3. Flow chart of the proposed framework for this work. The framework comprises three core modules, including the DEM generation module, difference DEM processing module and the mass balance analysis module.

3. Methods

In this study, we developed a three-module framework to generate and analyze glacier elevation change rates (dh/dt) and mass balance in Karakoram (Fig. 3). Module 1 focuses on generating temporally accurate DEMs from individual TanDEM-X acquisitions, providing the basis for calculating elevation changes. Module 2 involves creating differential DEMs (dDEMs) by combining seasonal DEM mosaics, which are used to derive the dh/dt and mass balance. Module 3 estimates the uncertainties in dh/dt and mass balance using a non-stationary spatial framework following the method proposed by Hugonnet et al. (2022). The final output includes a regional dataset of glacier dh/dt and mass balance estimation. The following sections describe the details of each module.

3.1. DEM generation

This section describes the detailed steps for DEM generation using a single TanDEM-X CoSSC product. The primary goal is to produce a temporally accurate DEM for each acquisition through an iterative refinement process, which ensures precise geocoding and reduces phase unwrapping errors using the residual phase derived from the CoSSC interferogram and a reference topography (Schweisshelm and Lachaise, 2022).

3.1.1. Residual phase decomposition

In DEM generation, the key component of the method is the residual phase between the CoSSC interferogram and the reference topography. Given an interferogram I_{CoSSC} calculated from a CoSSC product and I_{ref} simulated from the reference DEM, the residual phase can be expressed as:

$$\delta\varphi = I_{\mathrm{CoSSC}} - I_{\mathrm{ref}} \tag{1}$$

Ideally, after phase unwrapping, the residual phase $\delta\varphi$ would contain only the elevation difference between the CoSSC measurement and the reference topography. However, due to the presence of additional practical error sources, the residual phase $\delta\varphi$ should be further decomposed into the following components:

$$\delta\varphi = \delta\varphi_{\Delta h} + \delta\varphi_{\mathrm{miscal}} + \delta\varphi_{\mathrm{noise}} + \delta\varphi_{\mathrm{error}} \tag{2}$$

where $\delta\varphi_{\Delta h}$ is the phase related to the topographic height difference, $\delta\varphi_{\mathrm{miscal}}$ represents phase contributions from orbit mis-calibration, $\delta\varphi_{\mathrm{noise}}$ corresponds to incoherent noise in the CoSSC data and noise in the reference DEM, and $\delta\varphi_{\mathrm{error}}$ accounts for phase unwrapping errors.

Accurately estimating the elevation difference to refine the reference topography requires proper isolation of the phase term $\delta\varphi_{\Delta h}$ from the other error terms. To achieve this isolation, we developed a series of interferometric SAR (InSAR) processing steps, which are detailed in the following section.

3.1.2. InSAR processing

Before starting the InSAR processing steps, we geocoded the CoSSC images using the reference DEM to obtain an initial Look-Up Table (LUT) that converts SAR slant-range coordinates into DEM map coordinates. The geocoding process also generates the first simulated interferogram I_{ref} from the reference DEM, which is used to calculate the wrapped residual phase $\delta\varphi$.

To isolate the phase term $\delta\varphi_{\Delta h}$ from other error terms, we first used the LUT to inversely geocode the wrapped residual phase $\delta\varphi$ back into the map geometry. This step is crucial in mountainous regions to minimize unwrapping errors caused by extreme topographic features, such as steep slopes and sharp mountain peaks. Under the map geometry, we applied a coherence mask with a threshold value of 0.3 and masked out layover and shadow areas to eliminate unreliable phase data. The remaining phase data were then unwrapped using the Minimum-Cost-Flow (MCF) algorithm. To reduce phase jumps caused by large data voids, data gaps were filled with random noise prior to unwrapping. While this may introduce artifacts, it stabilizes the unwrapping process when data gaps are unavoidable.

After phase unwrapping, a quadratic polynomial phase model was fitted to the unwrapped phase map to estimate and remove phase trends caused by orbit mis-calibration. The fitted phase trend was subtracted from the unwrapped phase map, resulting in a preliminary phase map. However, extreme phase values caused by unwrapping errors may still be present and could propagate into the height difference maps. To address this, we converted the preliminary phase map into height differences Δh and created an extreme height mask to filter out unreliable phase pixels. The extreme height mask was generated by applying a threshold of $|\Delta h| > \min(10, 3\sigma_{\Delta h})$, where $\sigma_{\Delta h}$ is the standard deviation of Δh. After applying the extreme height mask, we refitted the quadratic phase model on the masked phase map and subtracted the newly fitted phase trend. This produced the corrected phase map, which successfully isolated the phase term $\delta\varphi_{\Delta h}$. Finally, the corrected phase map was converted into a height difference map Δh, which was used to update the reference DEM.

3.1.3. Iterative reference DEM update

In the previous step, we obtained a height difference map Δh representing the topographic height difference between the CoSSC measurement and the reference DEM. This difference arises not only from actual topographic change but also from geocoding errors introduced by the inaccurate LUT (Leinss and Bernhard, 2021). To separate

Table 1
Comparison of seasonal DEM mosaics over stable ground before and after co-registration.

		2011 Winter	2019 Winter
Before	Mean ± Std (m)	-1.460 ± 10.555	0.974 ± 8.554
	Median ± NMAD (m)	-1.112 ± 8.891	0.486 ± 7.058
After	Mean ± Std (m)	0.016 ± 6.893	-0.244 ± 5.759
	Median ± NMAD (m)	0.016 ± 2.456	-0.044 ± 2.183

the geocoding error from the actual topographic change, an iterative refinement process was applied.

In the first iteration, the initial reference DEM H_0 was updated using the height difference map Δh_1 derived from the InSAR processing steps, resulting in a corrected DEM $H_1 = H_0 + \Delta h_1$. The corrected DEM H_1 was then used to regenerate a new LUT with reduced geocoding errors. Following the same InSAR processing steps, a new height difference map Δh_2 was obtained from the corrected DEM.

In the second iteration, the DEM H_1 was updated using the new height difference map Δh_2, producing a second corrected DEM $H_2 = H_1 + \Delta h_2$. As the updated LUT from the previous iteration had already minimized geocoding errors, the geocoding step was no longer necessary. Instead, the corrected DEM H_2 was directly used to generate the simulated interferogram and calculate the residual phase. Following the InSAR processing steps, a new height difference map Δh_3 was obtained, representing the topographic difference between the CoSSC measurement and the second corrected DEM H_2.

After two iterations, geocoding errors were sufficiently reduced, and the final DEM H_3 was generated by updating the second corrected DEM H_2 with the new height difference map Δh_3:

$$H_3 = H_2 + \Delta h_3$$

This iterative process ensured that the final DEM was both accurate and free from significant geocoding errors.

3.2. Difference DEM processing

The individual DEMs generated from the CoSSC products were used as input in the second module for dDEM processing. This module involved a series of steps to create the regional dDEM map, including DEM mosaicking, coregistration, dh/dt calculation, outlier removal, and void filling.

3.2.1. Mapping the elevation change rate

To calculate the elevation change rate, the DEMs of the two study periods (2011–2012 and 2019–2020) were firstly merged to generate two seasonal DEM mosaics. Individual DEMs were re-projected onto a common grid aligned with the reference DEM to ensure proper pixel alignment. For overlapping pixels within the same grid cell, we applied a mean-merge strategy and calculated the average value of all overlapping pixels for the same grid cell. Each seasonal DEM mosaic was then co-registered to the reference DEM using the method proposed by Nuth and Kääb (2011). This step effectively reduced residual elevation errors caused by minor differences in geocoding transformations among the individual DEMs. As summarized in Table 1, co-registration have greatly improved the alignment between the seasonal mosaic and the reference DEM. For the 2011 winter DEM, the median elevation difference over stable regions decreased from −1.112 m to 0.016 m, with the Normalized Median Absolute Deviation (NMAD) decreased from 8.891 m to 2.456 m. Similarly, the median difference for the 2019 winter DEM was reduced from 0.486 m (NMAD: 7.058 m) to −0.044 m (NMAD: 2.183 m).

Using the two seasonal DEM mosaics, we generated the dDEM map by subtracting the 2011 winter DEM mosaic from the 2019 winter mosaic. The dh/dt map was then calculated by dividing the dDEM by the time difference between the two mosaics. Instead of using a fixed time interval, we calculated the interval for each pixel based on the timestamps of the individual DEMs used in the mosaics. This approach preserved the temporal accuracy of the dDEM and avoided ambiguities that might arise from using a fixed interval. Outliers in the dh/dt map were identified using an elevation binning method (Berthier and Brun, 2019). For each 100-m elevation bin, values deviating by more than ±3 NMAD from the median were masked as outliers. Pixels on slopes steeper than 40° were excluded from the calculation of median and NMAD values within each bin to reduce the impact of unreliable measurements.

3.2.2. Voids filling using Gaussian process regression

The generated dh/dt map exhibited substantial data gaps, primarily due to insufficient SAR acquisitions during the study period, low coherence in certain regions, and geometric effects such as layover and shadow. To ensure temporal consistency in the dh/dt map, we did not use DEMs from other years for void filling, as this could introduce temporal mismatches and ambiguity. Although hypsometric interpolation is a widely used alternative (McNabb et al., 2019; Berthier and Brun, 2019; Lv et al., 2020; Hugonnet et al., 2021), it often fails to accurately reconstruct large voids, particularly in complex glacier systems like those in the Karakoram.

To address these challenges, we adopted GPR for void filling, leveraging its ability to model spatially correlated data and to quantify prediction uncertainty (Williams and Rasmussen, 1995). Unlike deterministic interpolation methods, GPR provides both mean predictions and associated uncertainty estimates, thereby enhancing the interpretability and reliability of the reconstructed dh/dt values.

Given the strong influence of topography on glacier elevation changes, we modeled dh/dt as a function of several observable features, including the absolute elevation (h), terrain slope (α), aspect (θ), and spatial coordinates (x, y). The relationship is expressed as:

$$dh/dt = f(h, \alpha, \theta, x, y) + \epsilon \tag{3}$$

where $\epsilon \sim \mathcal{N}(0, \sigma^2)$ is the residual Gaussian noise. The function $f(\cdot)$ can be expressed as a Gaussian process defined by its mean function $m(\mathbf{X})$ and covariance function $k(\mathbf{X}, \mathbf{X}')$:

$$f(\mathbf{X}) \sim \mathcal{GP}(m(\mathbf{X}), k(\mathbf{X}, \mathbf{X}')) \tag{4}$$

where $\mathbf{X} = [h, \alpha, \theta, x, y]$ is the input feature vector. These features were selected based on their established relevance to glacier surface processes; however, future work could explore additional predictors such as curvature or distance from glacier centerline.

For the mean function, we set $m(\mathbf{X}) = 0$. The covariance function was defined as a sum of a Radial Basis Function (RBF) kernel and a Matérn kernel with $\nu = 1.5$, allowing the model to capture both smooth, large-scale and moderate, local variations in dh/dt. This hybrid kernel configuration was chosen based on preliminary experiments and previous literature, which indicate improved flexibility for representing glacier surface variability.

To account for glacier-specific dynamics, we trained a separate GPR model for each glacier. For each glacier, a stack of gridded features $(h, \alpha, \theta, x, y)$ was extracted from the reference DEM, paired with corresponding observed dh/dt values. Only pixels with measured dh/dt were used for model training and validation, while pixels with missing values were reserved for inference. To minimize spatial autocorrelation between training and validation sets, we employed a spatially stratified split: 80% of available pixels were randomly selected for training and 20% for validation, ensuring spatial independence where possible. To ensure computational efficiency, the training and validation sets were capped at 30,000 and 3000 pixels, respectively. All input features and target values were standardized to zero mean and unit variance prior to modeling.

The GPR models were trained by maximizing the exact marginal log likelihood (MLL), using the Adam optimizer with a learning rate of 0.01

and a maximum of 1000 epochs. Early stopping was applied with a patience threshold of 100 epochs, based on validation root-mean-squared error (RMSE). We set a fixed random seed for reproducibility and used gpytorch for model implementation, leveraging GPU acceleration to reduce computation time (Gardner et al., 2021). Model performance was primarily evaluated using RMSE on the validation set. We also computed mean absolute error (MAE) and coefficient of determination (R^2) to provide a more comprehensive assessment.

After training, the GPR model was used to infer both the mean and standard deviation of dh/dt in void regions. This probabilistic approach ensured that the void-filled dh/dt map not only reconstructed missing values but also provided pixel-wise uncertainty estimates, thus improving the reliability and interpretability of the final product.

3.3. Glacier mass balance analysis

Using the measured dh/dt map, the glacier-wide specific mass balance ($\bar{b}$) was calculated for individual glaciers in the study region. To avoid unreliable calculations, we limited the mass balance analysis to glaciers with an area larger than 1 km^2 and a minimum measurement coverage ratio of 30%. This resulted in 681 glaciers included in the analysis, with a total area of 10963.29 km^2.

For each glacier, the specific mass balance of glacier i is calculated using the mean dh/dt ($\overline{\frac{dh}{dt}}$) over the glacier, as expressed in Eq. (5):

$$\bar{b}_i = \rho \cdot \frac{1}{N} \sum_{i=1}^{N} \frac{dh}{dt}_i \tag{5}$$

where $\rho = 850 \pm 60$ kg/m^3 is the volume-to-mass conversion factor (Huss, 2013), N is the number of pixels within the glacier outline obtained from the RGI v7.0 dataset, and $\left(\frac{dh}{dt}\right)_i$ is the dh/dt value at pixel i.

The regional mass balance was calculated using the area-weighted mean dh/dt of all glaciers in the study region, as expressed in Eq. (6):

$$\bar{b}_{\text{region}} = \rho \cdot \frac{\sum_i^N A_i \cdot \overline{\frac{dh}{dt}}_i}{\sum_i^N A_i} \tag{6}$$

where A_i is the area of glacier i, $\overline{\frac{dh}{dt}}_i$ is the mean dh/dt of glacier i and N is the number of glaciers in the study region.

3.3.1. Glacier-wide uncertainty propagation

The uncertainty of the glacier-wide mass balance was calculated considering the uncertainty of the mean dh/dt per glacier and the uncertainty of the volume-to-mass conversion factor, as defined in Eq. (7):

$$\sigma_{\bar{b}}^2 = \left(\rho \cdot \sigma_{\overline{dh}}\right)^2 + \left(\overline{dh} \cdot \sigma_\rho\right)^2 \tag{7}$$

where $\sigma_{\overline{dh}}$ is the uncertainty of the mean dh/dt per glacier, and $\sigma_\rho = 60$ kg/m^3 is the uncertainty of the volume-to-mass conversion factor (Huss, 2013).

In Eq. (7), the uncertainty of the glacier-wide mean dh/dt ($\sigma_{\overline{dh}}$) can be further divided into two components, including the uncertainty of the measured region $\mathcal{M}$ and the voids filled region $\mathcal{V}$, as expressed in Eq. (8), assuming the two uncertainties are independent:

$$\sigma^2_{\overline{dh},\mathcal{G}} = \left(\frac{A_\mathcal{M}}{A_\mathcal{G}}\sigma_{\overline{dh},\mathcal{M}}\right)^2 + \left(\frac{A_\mathcal{V}}{A_\mathcal{G}}\sigma_{\overline{dh},\mathcal{V}}\right)^2 \tag{8}$$

where $A_\mathcal{M}$ and $A_\mathcal{V}$ are the areas of the measured and voids filled regions, respectively, and $A_\mathcal{G}$ is the total glacier area.

3.3.2. Uncertainty propagation in measured regions

To quantify the uncertainty of the mean dh/dt in the measured region $\mathcal{M}$, we employed a non-stationary spatial framework proposed by Hugonnet et al. (2022). This framework comprises three steps: standardizing errors, modeling spatial correlation, and propagating uncertainty.

Firstly, we used non-glaciated regions as proxies to quantify the systematic bias and random errors in dh/dt, with the assumption that elevation changes in these regions are negligible. By calculating the median and NMAD of dh/dt over the non-glaciated regions, we found that the median dh/dt value was −0.00024 m yr^{-1}, and the NMAD of dh/dt was 0.20 m yr^{-1}. These indicates negligible systematic bias and relatively low uncertainties in the dh/dt measurements. However, we must consider the heteroskedasticity of the dh/dt dispersion before modeling the spatial correlation of random errors (Hugonnet et al., 2022). Using the proxy errors, we modeled the dependence of elevation change errors on terrain slopes with an exponential curve, fitting the model using the average NMAD of dh/dt across 1-degree slope bins. Based on the heteroskedasticity model, we standardized dh/dt following Eq. (9):

$$Z_{dh/dt} = \frac{dh/dt}{\sigma_{dh/dt}} \tag{9}$$

where $\sigma_{dh/dt}$ represents the modeled dispersion of dh/dt and $Z_{dh/dt}$ is the standardized dh/dt.

Secondly, the spatial correlations of dh/dt uncertainties was modeled using $Z_{dh/dt}$. To model the spatial correlation, we employed the Dowd estimator and derived the empirical variogram from the stable region. A variogram quantifies how data similarity decreases as the distance between data points increases. The Dowd estimator is expressed in Eq. (10),

$$2\hat{\gamma}_{Z_{dh/dt}}(d) = 2.198 \cdot \text{median}\left(z(x,y) - z(x',y')\right)^2, \tag{10}$$

where $Z_{dh/dt}$ is the standardized dh/dt, and $z(x,y)$ and $z(x',y')$ are the standardized dh/dt of two sampled points with distance d (Dowd, 1984). Points in the estimator were sampled using a pairwise subsampling method proposed by Hugonnet et al. (2022). Compared to the classical Matern estimator, the Dowd estimator is less sensitive to outliers. Using the estimated variogram $\hat{\gamma}$, a spatially continuous variogram γ was fitted using a long–short range model, in which a Gaussian model and a Spherical model were employed to account for the short and long range correlations, respectively.

Finally, with the continuous variogram model γ, the uncertainties for the mean dh/dt of a glacier can be propagated using an exact analytical solution as shown in Eq. (11):

$$\sigma^2_{\overline{dh}} = \frac{1}{N^2} \sum_{i=1}^{N} \sum_{j=1}^{N} \sigma_i \sigma_j \left(1 - \gamma(d_{ij})\right) \tag{11}$$

where N is the number of pixels within the glacier outline, σ_i and σ_j are uncertainties of dh/dt at pixel i and j, respectively, and d_{ij} is the distance between pixel i and j. However, this analytical solution is computationally expensive for large glaciers. To address this, an approximate method proposed by Hugonnet et al. (2022) was adopted to reduce the computational cost while maintaining accuracy. This approximation uses a random subset of K pixels and is expressed as:

$$\sigma^2_{\overline{dh}} \approx \frac{1}{N^2 \cdot K} \sum_{i=1}^{N} \sigma^2_{dh,i} \cdot \sum_{k=1}^{K} \sum_{i=1}^{N} \left(1 - \gamma(x_k - x_i)\right) \tag{12}$$

where K is a random subset with k pixels, and x_k and x_i are the locations of pixel k and i, respectively.

3.3.3. Uncertainty propagation in void regions

For the voids filled region $\mathcal{V}$, we used the covariance matrix of the GRP model $k(\mathbf{X}, \mathbf{X}')$ to propagate the uncertainty for the mean dh/dt of the voids filled region following Eq. (13):

$$\sigma^2_{\overline{dh},\mathcal{V}} = \frac{1}{N^2_{\mathcal{V}}} \sum_{i=1}^{N_{\mathcal{V}}} \sum_{j=1}^{N_{\mathcal{V}}} k(x_i, x_j) \tag{13}$$

where $N_{\mathcal{V}}$ is the number of pixels within the voids filled region. In practice, $k(x_i, x_j)$ on large glaciers was not feasible to calculate due to the large number of pixels. To address this, we used a random subset of K pixels to approximate the covariance matrix, assuming the covariance structure is stationary.

3.3.4. Regional mass balance uncertainty propagation

To propagate the mass balance uncertainty from glacier-wide to regional scale, the uncertainty of glacier areas (σ_{A_i}) needed to be included additional to the uncertainty of the mean dh/dt ($\sigma_{\overline{dh}}$) and the volume-to-mass conversion factor (σ_ρ). Assuming the three uncertainty sources are independent, the uncertainty of the regional mass balance can be expressed as:

$$\sigma^2_{b_{\text{region}}} = \left(\rho \cdot \sigma_{\overline{dh}_\Sigma}\right)^2 + \left(\overline{dh}_\Sigma \cdot \sigma_\rho\right)^2 \tag{14}$$

where $\sigma_{\overline{dh}_\Sigma}$ is the uncertainty of the area-weighted mean dh/dt of all glaciers in the study region.

The uncertainty of the area-weighted mean dh/dt can be calculated using the following equation:

$$\sigma^2_{\overline{dh}_\Sigma} = \frac{1}{(\sum A_i)^2} \left[\sum_i^N \left(\overline{dh}_i - \overline{dh}_\Sigma\right)^2 \sigma^2_{A_i} + \sum_i^N \sum_j^N A_i A_j \mathrm{Cov}(\overline{dh}_i, \overline{dh}_j) \right] \tag{15}$$

where $\overline{dh}_\Sigma$ is the area-weighted mean dh/dt of all glaciers in the study region, and $\mathrm{Cov}(\overline{dh}_i, \overline{dh}_j)$ is the covariance between the mean dh/dt of glacier i and glacier j. Using again the variogram model γ, the covariance can be expressed as:

$$\mathrm{Cov}(\overline{dh}_i, \overline{dh}_j) = \sigma_{\overline{dh}_i} \sigma_{\overline{dh}_j} - V \tag{16}$$

where $\sigma_{\overline{dh}_i}$ and $\sigma_{\overline{dh}_j}$ are the uncertainties of the glacier-wide mean dh/dt for glacier i and glacier j, respectively, and V is the variogram model. Detailed derivation of Eq. (16) can be found in Appendix A.

4. Results

4.1. Glacier surface elevation change

The spatial distribution of glacier dh/dt across the Karakoram region revealed a wide range of behaviors, with both thinning and thickening observed across the 681 glaciers analyzed (Fig. 4). The average dh/dt across the region was 0.0038 ± 0.0042 m yr^{-1} (STD = 1.18), while the median dh/dt was 0.036 m yr^{-1} (NMAD = 0.47). The observed variability reflected the complex interplay of climatic and dynamic processes affecting glaciers in this region.

The regions of maximum thickening and thinning are highlighted in Fig. 4(a). The maximum dh/dt value, 21.44 m yr^{-1}, was observed on the Hispar Glacier (RGI2000-v7.0-G-14-21670), specifically along the glacier trunk near its Kunyang Tributary. This corresponded to a documented surge event on the glacier's main trunk between 2013 and 2016, during which a maximum thickening of over 180 m was observed, aligning well with our dh/dt measurements (Guo et al., 2020). Conversely, the minimum dh/dt value, -10.27 m yr^{-1}, was found on the Panmah Glacier (RGI2000-v7.0-G-14-12063), near its tributaries. The observed high rates of thinning (dh/dt) were likely a result of reduced ice flux and increased ablation during the quiescent phase of the surge cycle. Historical records indicate that several surge events occurred on these tributaries between 1995 and 2005, prior to the study period (Hewitt, 2007). Following these surges, the glacier likely entered a quiescent phase during the study period. Another notable thinning region was found on the Siachen Glacier (RGI2000-v7.0-G-14-20040, Fig. 4(d)), with around $-3\sim-4$ m yr^{-1} of thinning. This anomalous elevation change was related to a rock avalanche event during 2001 and 2016 documented in Berthier and Brun (2019).

Table 2
Population size and area of glaciers in different surge categories.

Category	Population (%)	Area (km^2, %)
0 - No Evidence	523 (76.80%)	2159.69 (19.70%)
1 - Possible Surge	3 (0.44%)	22.44 (0.20%)
2 - Probable Surge	24 (3.51%)	440.56 (3.02%)
3 - Observed Surge	131 (19.23%)	8340.61 (76.08%)

In the Karakoram region, surge-type glaciers are widely distributed. Their unique behaviors, which distinguish them from non-surge glaciers, making the analysis of surge-type glaciers critical for understanding regional glacier dynamics (Quincey et al., 2011). Surge glaciers are typically characterized by rapid mass redistribution events, such as advancing ice fronts and thickened lower glacier regions, followed by a quiescent phase during which ice flux is reduced and ablation dominates. In this study, surge-type glaciers were identified using the RGI v7.0 database, where glaciers are classified as observed surge, probable surge, possible surge, and no-evidence (RGI Consortium, 2023). As summarized in Table 2, surge-type glaciers in the study region account for 19.23% of the total glacier population but cover 75.63% of the total glacier area. In contrast, non-surge glaciers make up 76.80% of the population but cover only 19.70% of the glaciated area. A comparison of surge-type and non-surge glaciers revealed distinct differences in their elevation change behaviors.

During the studied period, surge-type glaciers exhibited diversified thickening and thinning in their ablation (areas of ice loss, typically at lower elevations) and accumulation zones (areas of ice gain, typically at higher elevations). Glaciers in the active surge phase generally experienced thickening in accumulation zones and thinning in ablation zones. One notable example was the South Rimo Glacier (Fig. 4(b), black arrow), which entered its surge phase in 2013 and experienced maximum thickening of approximately 28 m at the surge front by 2019 (Li et al., 2021; Jiang et al., 2021). Another example was the North Kunchhang Glacier I (Fig. 4(c)), which underwent a documented surge between June 2015 and June 2019 (Zhao et al., 2025). Such strong surge dynamics significantly impacted glacier mass distribution, leading to high variability in dh/dt values for surge-type glaciers. In contrary, glaciers in the post-surge recovery phase, such as the Panmah Glacier, were mostly characterized by thinning in the ablation zones but limited thickening in the accumulation zones.

Statistical analysis further highlighted the differences between surge-type and non-surge glaciers. The mean dh/dt for all surge-type glaciers (including possible and probable surge glaciers) is 0.019 ± 0.0052 m yr^{-1} (STD = 1.32), and the median dh/dt is 0.068 m yr^{-1} (NMAD = 0.50). This variability was largely driven by the dynamic processes of surging, which cause localized thickening and thinning. In contrast, non-surge glaciers were primarily influenced by climatic factors such as temperature and precipitation, which drive gradual thinning. Their mean dh/dt was -0.058 ± 0.0044 m yr^{-1} (STD = 0.53), and the median dh/dt was -0.054 m yr^{-1} (NMAD = 0.35). The narrower range of variability in non-surge glaciers reflected their more stable response to climate forcing, as opposed to the highly variable behavior of surge-type glaciers.

Distinctive patterns were also observed on the elevation dependence of dh/dt for surge and non-surge glaciers. As shown in Fig. 5, the median and NMAD of dh/dt were calculated for every 100 m elevation bins to capture the variability of dh/dt across different elevations. For

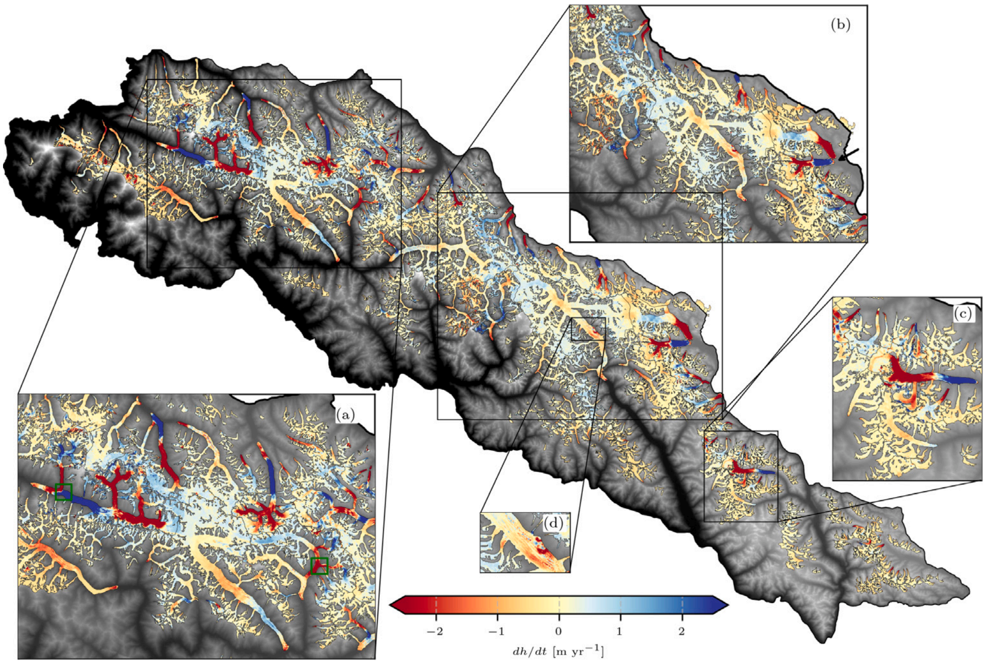

Fig. 4. Spatial distribution of glacier elevation changes in the study region. The base map in the background is the COP-30 DEM used as reference. dh/dt of individual glaciers are color-coded using the color bar. Insets are zoom-in views of sub-regions to offer a closer look of local details. Green boxes in the inset (a) indicate the location of observed maximum thickening and thinning. The black arrow in the inset (b) indicates the location of the Rimo Glacier.

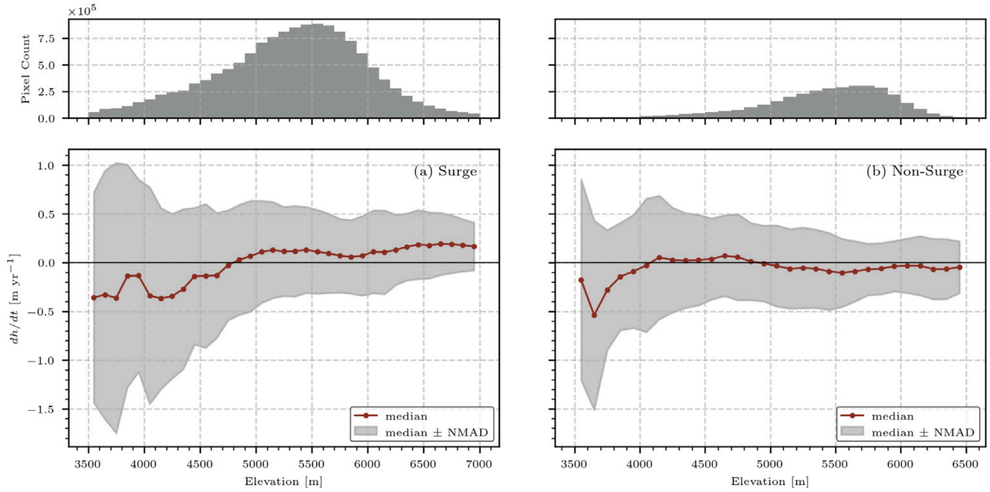

Fig. 5. Dependency of glacier dh/dt on elevation for surge-type (a) and non-surge (b) glaciers. The number of pixels within each elevation bin are shown with the bar plots on top panels. The median and Normalized Median Absolute Deviation (NMAD) values of each elevation bin are shown with the red line and gray shaded area.

surge glaciers, despite of the strong variability exhibiting in the data, a general transition altitude — where the median dh/dt approaches zero—was evident around 4700–4800 m a.s.l (above sea level). Below the transition altitude, the median dh/dt is predominantly negative, reflecting thinning in the ablation zones for most surge glaciers in the region. The magnitude of thinning decreased with increasing elevation, indicating a transition towards accumulation zones. Above the transition altitude, the median dh/dt stabilized around +0.1 m yr^{-1}, reflecting the thickening trend within most surge glaciers. For non-surge glaciers, a similar increasing trend as surge glaciers was observed for dh/dt with elevation increasing, but the transition altitude is located at a lower regions of approximately 4200–4300 m a.s.l. Below this altitude, dh/dt values were consistently negative, indicating thinning in the ablation zones. Above the transition altitude, dh/dt values fluctuate around zero, suggesting a near-balance between mass gain and loss in these higher-elevation areas.

4.2. Glacier mass balance

The area-weighted specific mass balance of the studied 681 glaciers was 0.0032 ± 0.0052 m w.e. yr^{-1}, showing a slightly positive mass balance for the region. However, the strong spatial variability of glacier dh/dt resulted in a highly heterogeneous distribution of glacier-wide specific mass balance across the study region (Fig. 6). Glaciers in the eastern extent of the study area (i.e., from 77.10 °E onward) generally exhibited negative mass balance. In contrast, glaciers in the central and north-western portions of the region are predominantly characterized by positive mass balance. However, a cluster of glaciers in the western

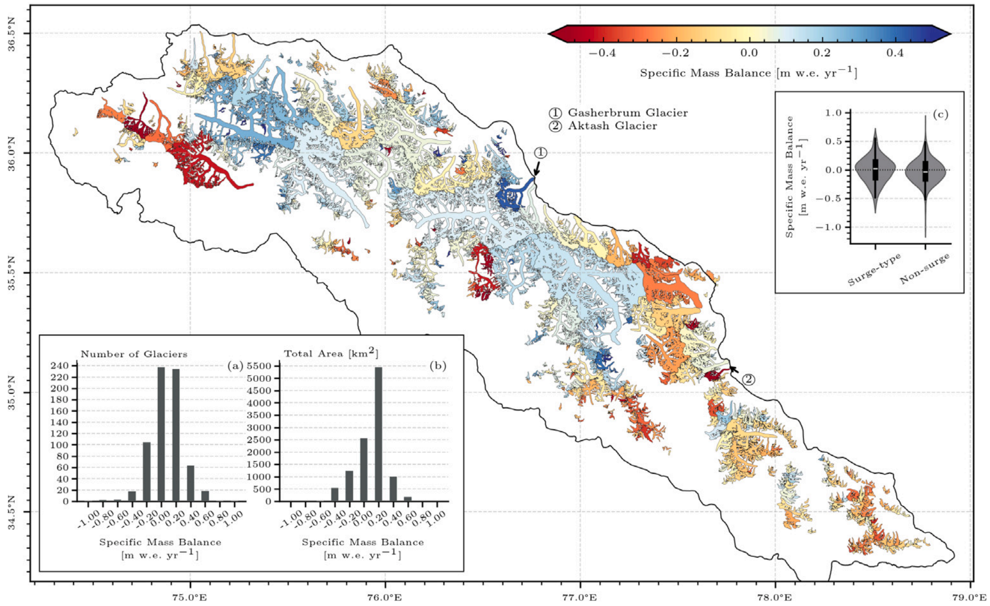

Fig. 6. Spatial distribution of glacier mass balance in the Karakoram region (main panel). The population size (a) and area (b) of glaciated regions are calculated for mass balance bins between −1 to 1 m w.e. yr^{-1}. Distribution of glacier mass balance for surge-type and non-surge glaciers are shown with the violin plot (c).

extent of the region (around 75.0 °E, 36.0 °N) experienced significant mass loss, standing out as localized exceptions to the overall trend.

Among glaciers larger than 10 km^2, the Gasherbrum Glacier (RGI 2000-v7.0-G-14-20459) showed the maximum mass gain, with a specific mass balance of 0.41 ± 0.044 m w.e. yr^{-1}. This glacier is a north-facing surge-type glacier with an area of 101.33 km^2. The most recent surge was observed between 2005 and 2007 and transited to its quiescent phase after 2008 (Usman and Furuya, 2018). While the exact reason for the substantial mass gain observed on the Gasherbrum Glacier remains unclear, it is likely resulted from the enhanced accumulation in the upper regions during the quiescent phase. In contrast, the glacier with the maximum mass loss is the Aktash Glacier (RGI2000-v7.0-G-14-18524), with a specific mass balance of -0.66 ± 0.070 m w.e. yr^{-1}. The Aktash Glacier is also a surge-type glacier, with an area of 24.43 km^2. Satellite imagery analysis reveals that this glacier has a relatively short surge cycle of approximately three years, with its most recent documented surge occurring between 2003/4 and 2009, advancing its terminus by more than 500 m (Bhambri et al., 2013). Approximate locations of the Gasherbrum and Aktash glaciers were marked on Fig. 6 with black arrows.

We analyzed the distribution of glacier population and area across different mass balance bins (Fig. 6(a) and (b)). The majority of glaciers have mass balance values within the range of −0.20 to 0.20 m w.e. yr^{-1}, with the peak population centered around 0.0 m w.e. yr^{-1}. However, the summed glacier area showed a clear bias towards positive mass balance. Specifically, more than 5000 km^2 of glacier area experienced slight mass gain of approximately 0.20 m w.e. yr^{-1}. This discrepancy between the distribution of glacier population and area was primarily attributed to the presence of large surge-type glaciers in the region. As illustrated in Fig. 6(c), surge-type glaciers exhibited a near balanced median mass change (0.0024 m w.e. yr^{-1}) and a density curve that skewed slightly towards positive. Their area-weighted specific mass balance is 0.0161 ± 0.0063 m w.e. yr^{-1}. This contrasted with non-surge glaciers, which had a negative median mass balance (−0.055 m w.e. yr^{-1}) and a slightly negative skewed density curve. The area-weighted specific mass balance for non-surge glaciers is -0.049 ± 0.0067 m w.e. yr^{-1}.

Two factors that may influence the individual glacier mass-balance variability were examined in Fig. 7, including glacier area and median elevation.

In the study region, the majority of glaciers fell within the smallest area category (1–5 km^2), and the number of glaciers decreased exponentially with increasing glacier area. Only 19 glaciers were in the largest category (100+ km^2). Smaller glaciers (1–5 km^2) exhibited a median thinning rate of approximately −0.01 m w.e. yr^{-1}, while larger glaciers showed relatively stronger thinner rate at around −0.05 m w.e. yr^{-1}. The largest glaciers (100+ km^2) displayed balanced mass change with the median value at approximately 0.02 m w.e. yr^{-1}). Despite the varying population of glaciers across area categories, the variance in individual glacier mass balance remained relatively consistent, with values generally ranging from −0.5 to 0.5 m w.e. yr^{-1}. While differences in skewness were observed among area categories, no clear trend towards positive or negative mass balance emerged.

For glacier median elevation, the majority of glaciers had median elevations above 5000 m a.s.l. A general stable near zero median mass balance were found for glaciers in groups of median elevations below 5400 m a.s.l., whereas strong median negative mass balance were found for glaciers in the group of median elevations above 5700 m a.s.l. Comparing to surge-type glaciers, the median mass balance of non-surge glaciers were closer to near zero. Similar to area categories (Fig. 7(a)), differences in skewness were observed across elevation groups, but no clear trend towards positive or negative mass balance was apparent.

4.3. Voids filling evaluation

Voids filling is a crucial step in regional dh/dt mapping and geodetic mass balance measurement (McNabb et al., 2019). This step was particularly important in our study, as we avoided using DEMs from different times for voids filling to ensure no temporal ambiguity was introduced, thereby leaving relatively large voids in the dh/dt map.

Given the complex terrain and glacier dynamics in the region, we employed the GPR model to infer the missing data in voids region, taking into account the dependence of dh/dt over various terrain features. Fig. 8 illustrated examples of voids filling for glaciers of varying sizes. In these examples, voids were predominantly located in high-elevation regions, typically within glacier accumulation zones or near glacier edges. High-elevation regions are often characterized by steep slopes and are affected by SAR image artifacts such as shadow and layovers, leading to data gaps in these areas. To fill the missing values in such

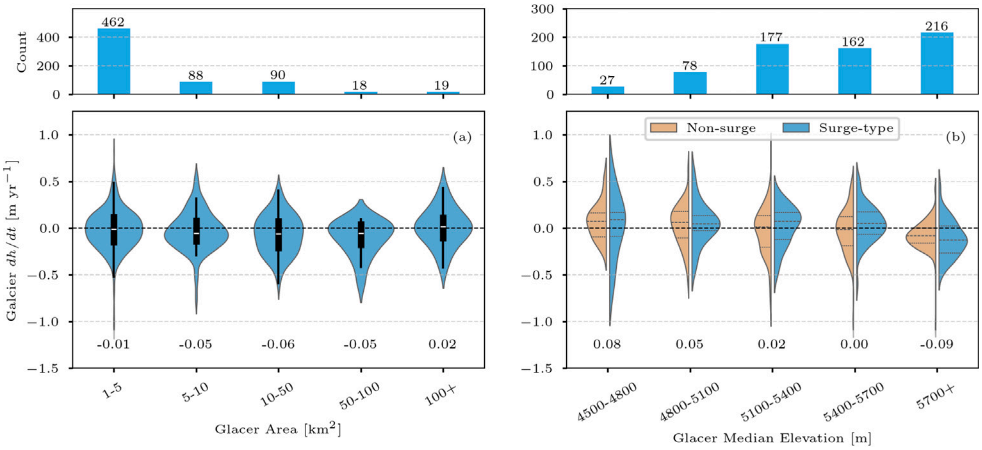

Fig. 7. Mass balance distribution with respect to different (a) glacier size groups and (b) glacier median elevation groups. The top panels show the count of glaciers within the respective group. The distribution of mass balance are calculated for the entire group in panel (a), and separately for surge-type and non-surge glaciers in panel (b).

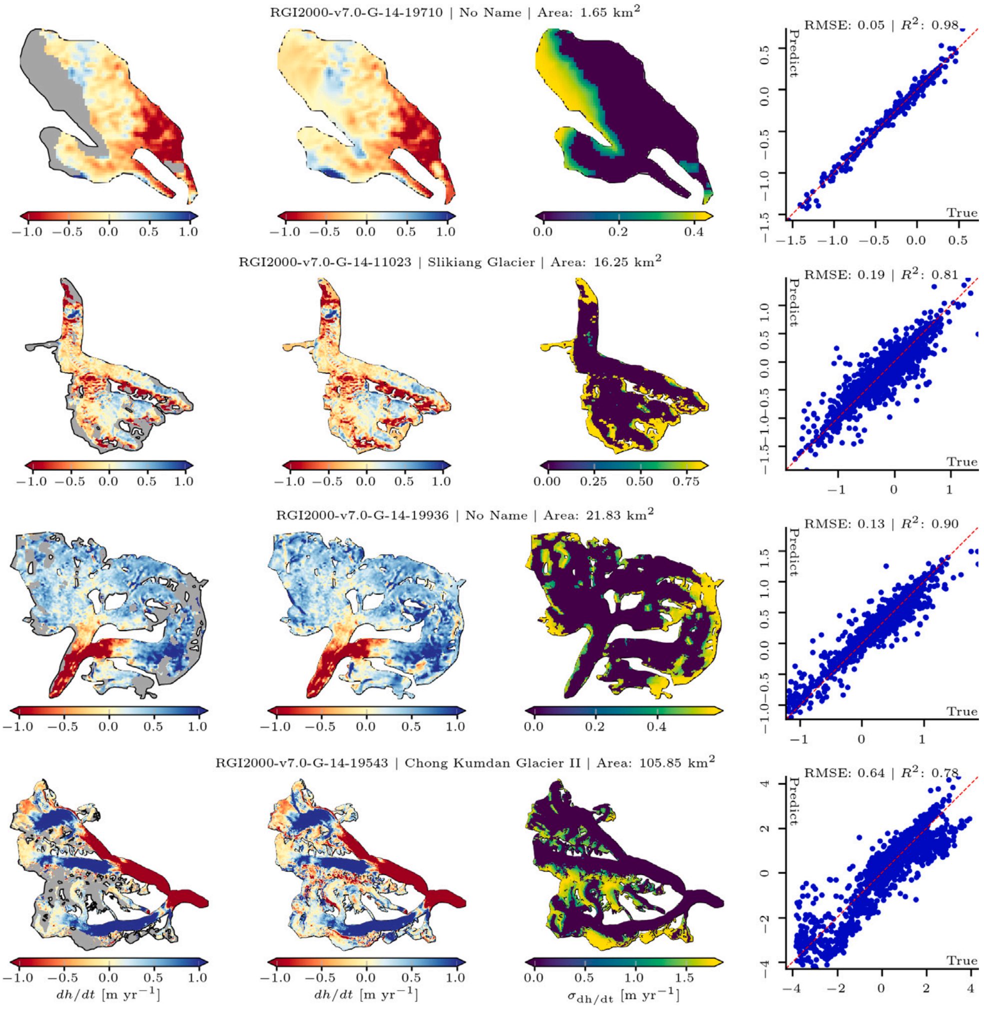

Fig. 8. Example glaciers demonstrate the voids filling performance using Gaussian Process Regression (GPR). The leftmost column show original glacier dh/dt maps with voids (marked as gray shaded). The second column show dh/dt maps with voids filled using GPR models. The third column shows the distribution of voids filling uncertainties, with zero representing the measured area (i.e. no filling). The rightmost column shows the validation performance of GPR models for the respective glacier, with blue scatter dots showing the validation pixels and red line showing the 1-to-1 matching. The RGI-index, name and area of the glacier are reported on top of the respective row. (For interpretation of the references to color in this figure legend, the reader is referred to the web version of this article.)

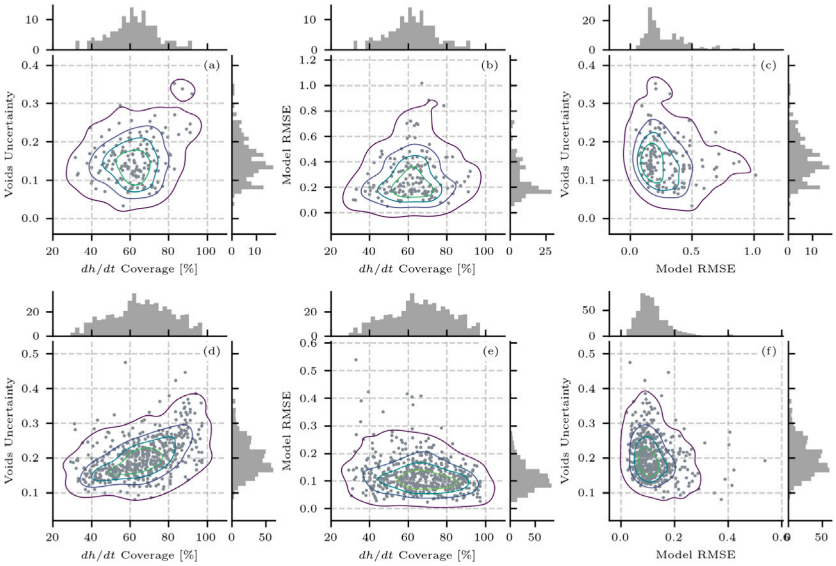

Fig. 9. Distribution of (left column) voids uncertainty versus dh/dt measurement coverage, (middle column) validation Root-Mean-Squared-Error (RMSE) versus dh/dt measurement coverage, and (right column) voids uncertainty versus validation RMSE for surge-type (top row) and non-surge (bottom row) glaciers.

regions, it is crucial to account for the spatial distribution of missing values and ensure that the interpolation method considers the influence of topography on the distribution of glacier elevation change.

Comparing to the original dh/dt map with voids (leftmost column), the filled dh/dt maps (second column) showed that the spatial patterns of dh/dt distribution were effectively reconstructed by the GPR model. The uncertainty in the filled regions, as shown in the third column, varied across glaciers. This variability was raised because the GPR models were trained for each glacier specifically, and the inference confidence of the model depended on several factors, including the quality of training data, the density of measured samples near prediction points, and the noise level in the data. Validation results (rightmost column) indicated that the model performs well for small glaciers (area below 5 km^2), achieving low RMSE and high R^2. For medium-sized glaciers, while the RMSE slightly increased, the R^2 remained high., indicating that the model continues to capture the dynamics effectively. For large glaciers, the validation RMSE showed only a moderate increase; however, the R^2 dropped below 0.8. This suggests that the model struggles to fully capture the more complex dynamics of large glaciers, which may be influenced by more diverse topographic conditions of large glaciers compared to smaller ones. Note that the validation results presented here are obtained by dividing the measured data for each glacier into separate training and validation sets, as described in Section 3.2.2. The model is trained only on the training data, and its predictive accuracy is then evaluated on the validation data—these are real measurements that were not used during training. This approach allows us to measure how well the GPR model can predict missing values based on available data.

As shown in Fig. 9, we inspected the relationship between voids uncertainty, dh/dt measurement coverage, and the validation RMSE of GPR models for both surge-type (top row) and non-surge (bottom row) glaciers. For surge-type glaciers, the distribution of voids uncertainty exhibited a relatively isotropic pattern with respect to measurement coverage, suggesting that voids uncertainty was not strongly correlated with the measurement coverage. Similarly, the model validation RMSE showed a uniform pattern across different levels of measurement coverage. When examining the relationship between voids uncertainty and RMSE (Fig. 9c), a slight inverse correlation was observed for RMSE values between 0.0–0.5, where higher RMSE corresponded to lower voids uncertainty. For larger RMSE values (above 0.5), voids uncertainty became independent from RMSE and was concentrated between 0.1–0.2. For non-surge glaciers, voids uncertainty showed a weak and noisy positive correlation with measurement coverage. The model validation RMSE, on the other hand, does not exhibit a clear dependence on measurement coverage, with contours spread uniformly across different coverage levels. Finally, the relationship between voids uncertainty and RMSE revealed no strong dependence, as the contours were relatively uniform and do not indicate a clear trend.

This result shows that the uncertainty over the voided region does not depend on the size of the voids, nor on the overall validation accuracy of the model. This is due to the fundamental principle of how GPR model estimates uncertainty for a target variable. In GPR modeling, each predicted value is treated as a random variable described by a probability distribution, rather than a single fixed value. The shape of this distribution is determined by a kernel function, which captures the spatial correlation among all available data samples. As a result, the uncertainty provided by the GPR model is mainly influenced by the spatial distribution of the measured data points within the feature space. In the feature space, if a missing value is surrounded by many relevant and similar measurements, the model will be more confident in its prediction, resulting in lower uncertainty. Conversely, if the missing value is isolated or located in an area with unusual terrain features, the uncertainty will be higher. By incorporating various terrain features as inputs to the GPR model, we ensured that the distribution of available measurement samples in the feature space remains independent of voids size and the distribution of training samples. Consequently, the model achieves robust inference for missing values in the voids region.

4.4. DEM accuracy and uncertainty propagation

To validate the accuracy of the seasonal DEM mosaics, we compared the 2019 winter mosaic with ICESat −2 measurements over glacier-free surfaces. The ICESat −2 points were acquired between 2019-08-29 and 2020-04-26 and matched the time span of the second acquisition period of the CoSSC products. Points over slopes steeper than 40° were excluded due to the high uncertainty of TanDEM-X measurements in such areas. A total of 58,777 ICESat −2 points with surface slopes between 0° and 40° were used for validation. The spatial distribution of the validation points is shown in Fig. 1. The comparison revealed that the ICESat −2 measurements were slightly higher than the generated DEM mosaic, with a mean difference of 0.29 m and a median difference of 0.28 m (Fig. 10). This discrepancy is likely due to the deeper penetration of SAR signals compared to ICESat −2 measurements (Abdullahi et al., 2019). The vertical accuracy of the DEM mosaic, estimated using

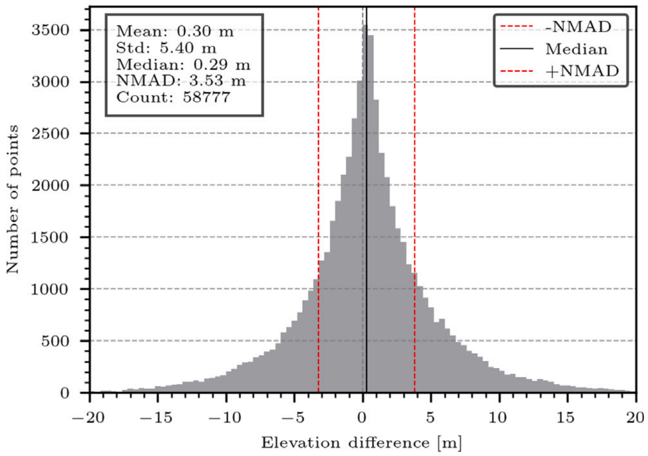

Fig. 10. Distribution of elevation differences over stable ground between ICESat −2 measurements and the 2019 winter DEM mosaic. The median and ± 1 Normalized Median Absolute Deviation (NMAD) values are indicated by the black solid lines and red dashed lines, respectively. (For interpretation of the references to color in this figure legend, the reader is referred to the web version of this article.)

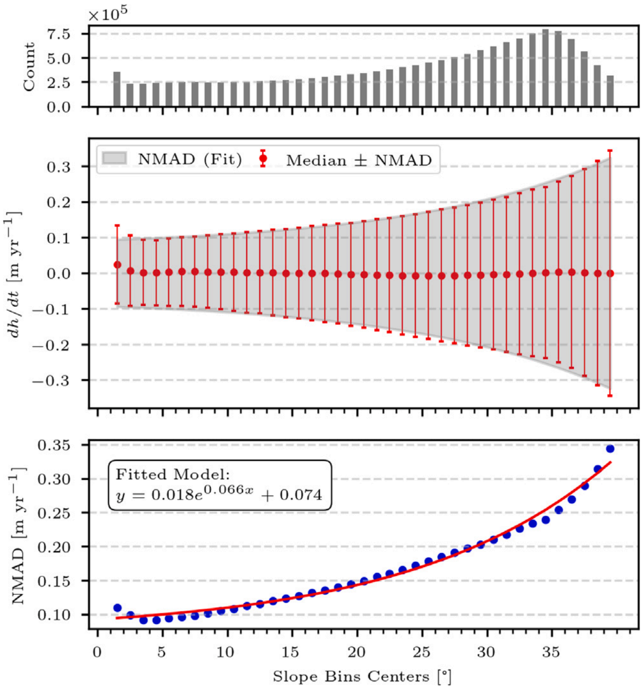

Fig. 11. The dependence of dh/dt uncertainty (dispersion) on terrain slope, derived from stable regions. The dispersion is quantified using the Normalized Median Absolute Deviation (NMAD). Top: number of pixels in each slope bin. Middle: the median dh/dt in each slope bin and the NMAD shown as error bars; The fitted NMAD for each slope bin are shown with the shaded area. Bottom: the NMAD of dh/dt in each slope bin (blue dots) and the fitted exponential function for the dispersion dependence on slope (red line). (For interpretation of the references to color in this figure legend, the reader is referred to the web version of this article.)

the NMAD of elevation differences, was 3.53 m. This accuracy is lower than the typical accuracy of the COP-30 DEM, likely due to the complex terrain in the study area and the absence of post-editing steps.

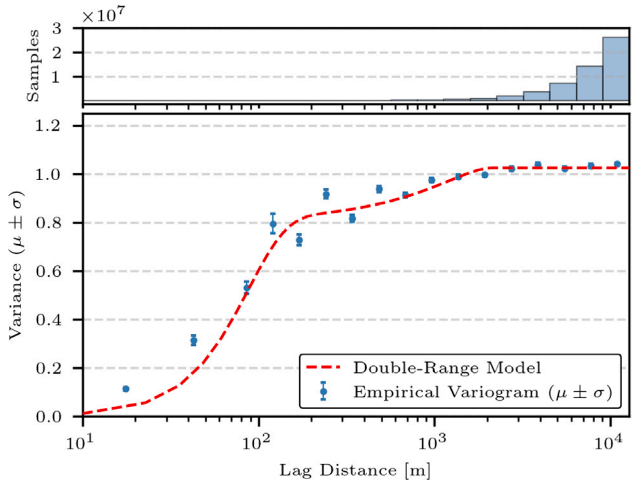

Fig. 12. Spatial correlation of dh/dt uncertainty inferred from the non-glaciated regions. The bottom panel shows the spatial variogram of standardized elevation differences. The empirical variogram is based on Dowd's estimator. The fitted variogram is the sum of a short-range Gaussian model and a long-range spherical model. The top panel shows the count of samples in each distance bins.

Besides the highly accurate DEM, we also rigorously analyzed the uncertainty of the measured dh/dt using a non-stationary framework. This approach accounts for the heteroskedasticity of measurement errors in dh/dt and incorporates spatial error correlations over both short and long ranges.

As illustrated in Fig. 11, we investigated the relationship between dh/dt and terrain slope across non-glaciated regions. These areas revealed a clear dependence of dh/dt dispersion on slope, which is captured by the modeled exponential curve expressed in Eq. (17):

$$\sigma_{dh/dt} = 0.018e^{(0.066\alpha)} + 0.074 \tag{17}$$

Here, $\sigma_{dh/dt}$ represents the dispersion of dh/dt and α denotes the terrain slope. This dependence can be attributed to the influence of local incidence angles on the sensitivity of the interferometric phase to elevation within the InSAR system. On steeper terrain, the precision of InSAR digital elevation models (DEMs) decreases, resulting in higher dh/dt dispersion and greater uncertainty.

To further refine the analysis, we standardized dh/dt using the modeled heteroskedasticity and employed non-glaciated regions as proxies to infer spatial error correlations. The empirical variogram and its fitted continuous variogram are presented in Fig. 12. The spatial correlation model combines a short-range Gaussian component and a long-range Spherical component. Specifically, the Gaussian model has a range of 204.53 m and a partial sill of 0.76; the Spherical model has a range of 1590.40 m and a partial sill of 0.28. These results indicate that short-range correlations dominate the standardized dh/dt errors, but long-range correlations remain considerable. As noted by Hugonnet et al. (2022), relying solely on short-range models may severely underestimate elevation uncertainties for areas larger than 0.1 km^2.

5. Discussion

5.1. Regional mass balance in karakoram

In Karakoram, the anomalous behavior of glacier mass balances has been identified since the 1970s, which was characterized by stable and weakly positive mass balance in the region in contrast to the mass loss observed in the Himalayas and other regions of the world (Hewitt, 2005; Farinotti et al., 2020). Benefiting from the increasingly available remote sensing data, geodetic mass balance measured by DEMs derived

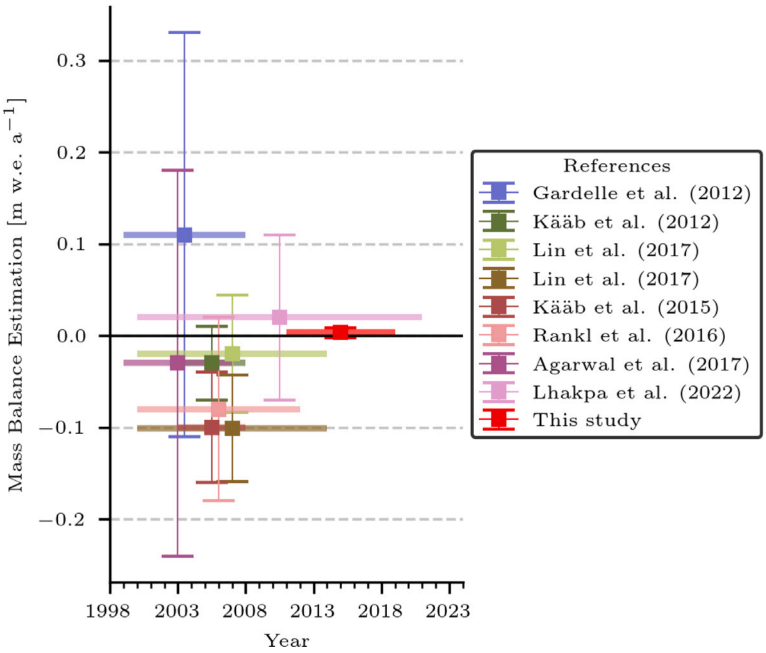

Fig. 13. Comparison of the regional specific mass balance reported in relevant studies and this study. The horizontal bars represent the time periods covered by each study, and vertical bars indicate the uncertainty. References include Gardelle et al. (2012), Kääb et al. (2012, 2015), Rankl and Braun (2016), Agarwal et al. (2017), Lin et al. (2017), Lhakpa et al. (2022). Result of this study is highlighted in red. The black solid line at 0 m w.e. yr^{-1} serves as a reference for no net mass change. (For interpretation of the references to color in this figure legend, the reader is referred to the web version of this article.)

using LiDAR, optical stereo image pair and SAR data have provided valuable information on the mass balance of glaciers in Karakoram.

A recent review by Li et al. (2023) summarized the changes of glacier mass balance in the Karakoram region since 1998 made by relevant studies (Fig. 13). Although these studies cover various temporal and spatial scales, the reported mean mass balance generally ranged between ± 0.1m w.e. yr^{-1}, indicating a near-equilibrium state for glaciers in the region. However, some recent global scale studies suggested that the anomaly of mass balance change in Karakoram was no longer as significant as before. For instance, the thickening of glaciers in central-western Asian was observed to be brought down to a generalized thinning in the late 2010s using large-scale ASTER DEMs (Hugonnet et al., 2021), with the mean elevation change rate decreased from -0.1 ± 0.17 m yr^{-1} during 2000–2004 to -0.23 ± 0.14 m yr^{-1} in 2015–2019. The decade mean dh/dt during 2000–2019 for the region was reported to be -0.16 ± 0.06 m yr^{-1}, approximately equivalent to a specific mass balance of -0.135 ± 0.02m w.e. yr^{-1} with the assumption of a density of $\sim 850 \pm 60$ kg m^{-3}. A similar observation was made in the community that estimates the global glacier mass changes (Zemp et al., 2025).

In our results, the regional mass balance over almost a decade (2011–2019) was estimated to be 0.0032 ± 0.0052 m w.e. yr^{-1}, demonstrating a near balance to positive trend comparing to previous studies (Fig. 13). Particularly, our area-weighted mass balance is strongly contrast to the negative value reported in the global scale studies. To further illustrate the difference between the results of our study and the previous work, we compared our glacier dh/dt measurements with the openly shared results from Hugonnet et al. (2021). The regional mass balance calculated using the Hugonnet dataset is -0.1138 m w.e. yr^{-1} for the same glaciers covered in our study. The uncertainty is not quantified as we do not have access to the spatial correlation model of the Hugonnet dataset. To understand the different mass balance for each glacier measured by our study and the Hugonnet dataset, detailed comparison is shown in Fig. 14. In the comparison, the histograms illustrate the overall distribution of glacier aggregated dh/dt for both studies. While the distributions were largely overlapped, both the glacier-wide mean and median dh/dt of our results were slightly biased towards more positive values compared to the Hugonnet dataset. Additionally, our results exhibited slightly broader tails, indicating higher variability in glacier aggregated dh/dt. As median values were more robust to outliers, the distribution of median dh/dt values showed much less variability in both studies compared to the mean dh/dt distributions. The scatter plots provided a one-to-one comparison of glacier samples between our study and the Hugonnet dataset. For both the mean and median dh/dt, the data points were generally centered around the 1:1 line, indicating overall agreement between the two studies. However, noticeable scatterings were present, highlighting the different distribution of glacier-wide dh/dt distributions.

A few example glaciers are presented in Fig. 15 to further illustrate the differences between the two datasets. For small and medium sized glaciers (Fig. 15(a) and (b)), both dh/dt maps showed consistent and comparable spatial patterns. For instance, strong thinning was observed at similar locations in both datasets. However, our results resolved finer-scale variations, such as crevasses and isolated zones of thinning and thickening, which were smoothed out in the Hugonnet dataset due to the coarser resolution. For surge-type glaciers (Fig. 15(c) and (d)), both studies captured the general thickening-thinning patterns along the main trunk of the glaciers. However, notable differences were observed in the accumulation zones. For the glacier in Fig. 15(c), our dh/dt map showed general positive elevation changes in the accumulation region, while the Hugonnet dataset exhibited substantial variability and large areas of negative elevation change. This discrepancy results in a positive glacier-wide mean dh/dt in our study, whereas the Hugonnet dataset yielded a negative mean dh/dt. A similar pattern was observed for the glacier in Fig. 15(d), where our results showed balanced or slightly positive elevation changes across the accumulation zone, and the Hugonnet dataset showed large variability with extensive areas of negative elevation changes.

The difference observed in the above comparison can be explained by the different data and methods used for the analysis. In the Hugonnet dataset, the elevation change was estimated using a multi-year time-series fitting approach with ASTER DEMs for the period 2000–2019. The dh/dt map for individual glaciers were provided with 100m resolution. In our study, we employed only the TanDEM-X data acquired

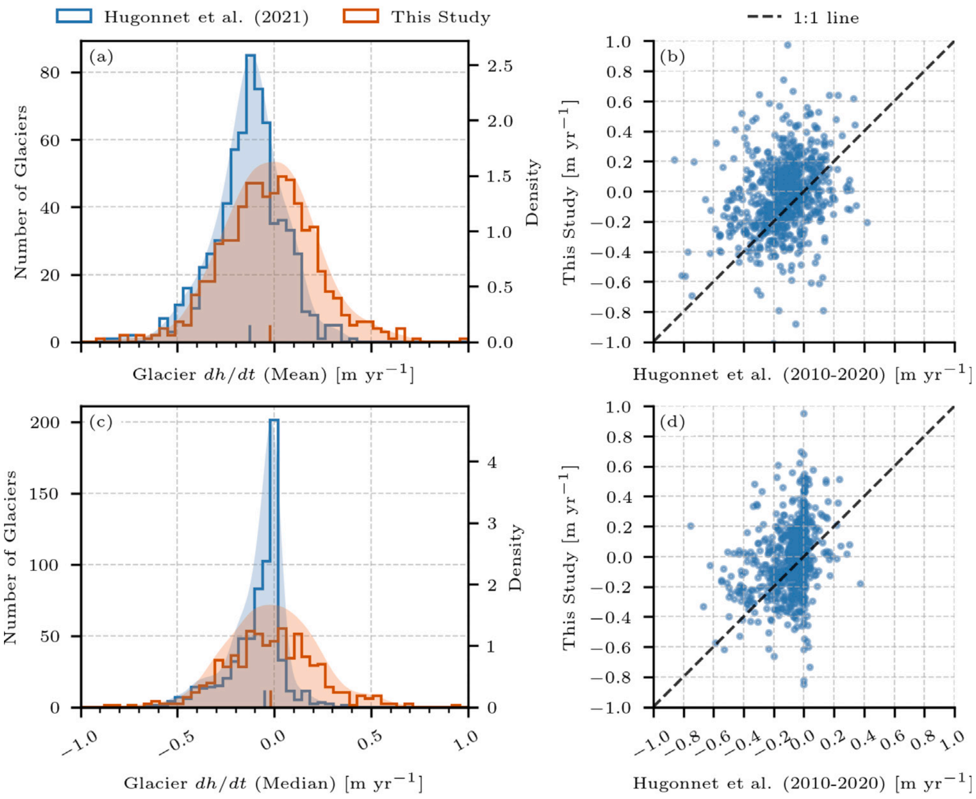

Fig. 14. Comparison of glacier elevation change rates (dh/dt) between this study and the Hugonnet et al. (2021) dataset. The top row and the bottom row shown the distribution of mean and median glacier dh/dt (a, c) and their scatterplot comparison (b, d), respectively. The histograms illustrate the number of glaciers and density for each dataset. The scatter plots include a 1:1 reference line for visual comparison.

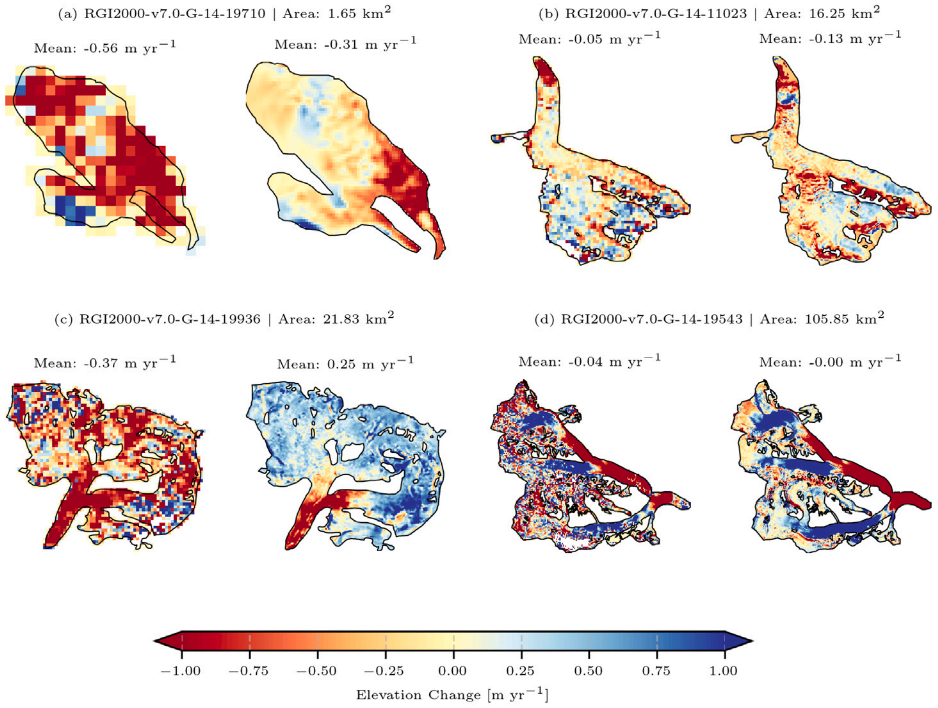

Fig. 15. Elevation change rate (dh/dt) for example glaciers of varying sizes derived from this study and the dataset of Hugonnet et al. (2021). For each glacier in (a)–(d), the left map represents results from the dataset of Hugonnet et al. (2021), and the right map corresponds to the results of this study. The mean dh/dt is indicated for each glacier. The color bar at the bottom illustrates the range of dh/dt.

in two operational phases (2011–2014 and 2015–2019) to avoid introducing artifacts caused by system bias and seasonal ambiguities. The former method is more robust in estimating the trend of mass changes, while our results preserved better temporal sensitivity and spatial variability. Besides, the Hugonnet dataset was produced using the ASTER DEM and relied on data interpolation to fill the spatial–temporal data gaps caused by cloud contamination. The interpolation process may introduce additional uncertainties and smooth out fine-scale spatial patterns, particularly in accumulation zones where elevation changes are generally smaller and more variable. In contrast, our use of TanDEM-X data, which offers stronger penetration capabilities through cloud, provides more reliable elevation measurements with less interference. Thus, the choice of data and processing methods may play a significant role in the reported mass balance differences. Considering the varying analysis performed in different studies, further investigation is needed to reconcile differences across studies, integrate diverse datasets and methodologies, and derive consensus estimates (Zemp et al., 2025).

5.2. Spatial variability of elevation and mass change

Benefiting from the high-resolution TanDEM-X CoSSC data, detailed maps of glacier dh/dt and mass balance were generated for over 10,000 km^2 of glacier covered area in Karakoram. The dh/dt map revealed the highly heterogeneous spatial distribution of glacier elevations changes in the region. From the dh/dt map, the spatial variability of elevations changes is observed to be predominantly contributed by the surge-type glaciers. Previous studies have reported that surging events in Karakoram were expanding and increasing, coincident with the positive glacier mass balance in the region (Copland et al., 2011). A similar observation was made in our study, where the statistical analysis on dh/dt showed that surge-type glaciers in the region are generally in a near-equilibrium or positive mass balance state, while non-surge glaciers mostly experienced thinning and mass loss. Another notable observation from the dh/dt map is the varied surge-phase that the surge-type glaciers experienced. Glaciers experiencing (or just finished) the active surge phase mostly have large thickening close to the glacier front and strong thinning in their accumulation zones. In contrary, glaciers in the quiescent or post-surge recovery phase generally showed thinning in their middle and lower parts, with thickening observed in the upper reach. Example surge-type glaciers of such contradicting behaviors can be found in Fig. 4(b).

Besides the spatial heterogeneity, the distribution of elevation change along altitude also demonstrates distinctive behavior between surge-type and non-surge glaciers. Overall, both glacier types exhibit a similar trend of decreased thinning rates with increasing elevation. This altitude-dependent pattern has been widely documented in previous studies (Gardelle et al., 2013-08-09; Brun et al., 2017; Ragettli et al., 2016-09-14), and reflects the transition from ablation zones, where mass loss dominates, to accumulation zones, where mass gain increases. The thickening or near-balanced state observed at higher elevations may serve as an indicator of the overall mass balance condition. However, our results reveal a notable difference in between surge and non-surge glaciers. The transition altitude for surge glaciers is located at a higher altitude (4700–4800 m a.s.l.) compared to non-surge glaciers (4200–4300 m a.s.l.), suggesting distinct mass balance regimes influenced by glacier dynamics. Moreover, the altitude dependence of elevation change is known to be strongly influenced by localized glacier dynamics, morphological features, and climate regimes (Brun et al., 2017). For instance, thick debris cover or delayed adjustment to balance velocities could alter thinning or thickening trends at specific elevations, as observed in other regions such as Bhutan and Kunlun (Brun et al., 2017). These localized factors highlight the complexity of interpreting elevation-dependent mass balance trends across large regions. Further investigation, particularly through coupling with glaciological models, could provide deeper insights into the elevation dependence of glacier mass balance (Cogley, 2009).

It is important to note that the classification of surge-type glaciers in our analysis is based on the RGI 7.0 inventory, which may not fully capture the timing of individual surging events relative to our study period. Glacier surges are episodic and can occur outside the temporal window of our elevation change measurements, potentially leading to mismatches between the cataloged surge status and actual glacier dynamics during our observation timeframe. This limitation should be considered when interpreting the observed differences between surge and non-surge glaciers, as the surging activity may not be contemporaneous with our data. Future studies incorporating time-resolved surge inventories or direct monitoring of glacier dynamics would help to more accurately assess the impact of surging behavior on elevation change patterns.

Due to the strong variability of regional dh/dt, the mass balance of glaciers in Karakoram is also highly heterogeneous. From the mass balance map (Fig. 6), a general trend of mass balance change can be observed, with thinning in the eastern and thickening in the western part of the region. A similar finding was reported by Berthier and Brun (2019), where the mass balance in the central and western part of the region showed stable to positive mass balance, with statistically significant difference to the eastern part. However, in our study, the longitude dividing the change of mass balance appeared to be around 77.1 °E, which is slightly different from the 76.5 °E reported by Berthier and Brun (2019). This difference is likely due to the different mass balance of the Siachen Glacier between the two studied period (2011–2019 vs 2000–2016).

Another factor contributing to the heterogeneous pattern of mass balance in the Karakoram is the extensive presence of debris-covered glaciers. Based on the survey of Herreid and Pellicciotti (2020-09-02), the debris covered area accounts for approximately 17% of all glaciated area within the studied glaciers. One example of anomalous mass balance caused by debris-covered glaciers can be observed in the western part of the region (around 75 °E, 36 °N). As shown in Fig. 16, dh/dt on debris-covered regions show slightly right skewed distribution compared to non debris-covered areas, with the mean dh/dt of 0.01 m yr^{-1} (SD=2.47 m yr^{-1}) and median of −0.20 m yr^{-1} (NMAD=0.90 m yr^{-1}). In contrast, the mean dh/dt on non debris-covered areas is 0.00 m yr^{-1} (SD=0.89 m yr^{-1}) and median of 0.05 m yr^{-1} (NMAD=0.43 m yr^{-1}). The difference in dh/dt distribution between debris-covered and clean-ice glaciers is statistically significant based on the two-sample Kolmogorov–Smirnov test ($p < 0.0001$). According to Herreid and Pellicciotti (2020-09-02), the area of debris-covered glaciers in the entire South Asia West is approximately 3662 km^2, accounting for 13.7% of the total glaciated area in the region. On debris-covered glaciers, field surveys and modeling studies have shown that thick debris layers can reduce ice melt rates by insulating the glacier surface and limiting thermal energy transfer, whereas thin and moist debris layers can accelerate ablation by increasing the absorption of solar radiation (Scherler et al., 2011; Mayer and Licciulli, 2021; Huo et al., 2021). The complex interactions between debris cover characteristics, glacier dynamics, and local climate conditions contribute to the observed heterogeneity in mass balance patterns across the Karakoram region.

5.3. Uncertainty of the mass balance estimation

In this study, we implemented a nonstationary heterogeneous framework to quantify uncertainties in glacier elevation change and mass balance estimations. By employing glacier-free terrain as proxies, we effectively modeled both the heteroskedasticity of dh/dt measurement errors and their spatial correlation patterns. This approach ensured proper consideration of slope-dependent random errors and the correlation of errors in both short and long-range distances.

Our analysis revealed remarkably precise results, with the uncertainty of mean glacier dh/dt across the entire region measuring ± 0.0042 m yr^{-1}, and the uncertainty in regional specific mass balance at ± 0.0052 m w.e. yr^{-1}. These uncertainty values are approximately one

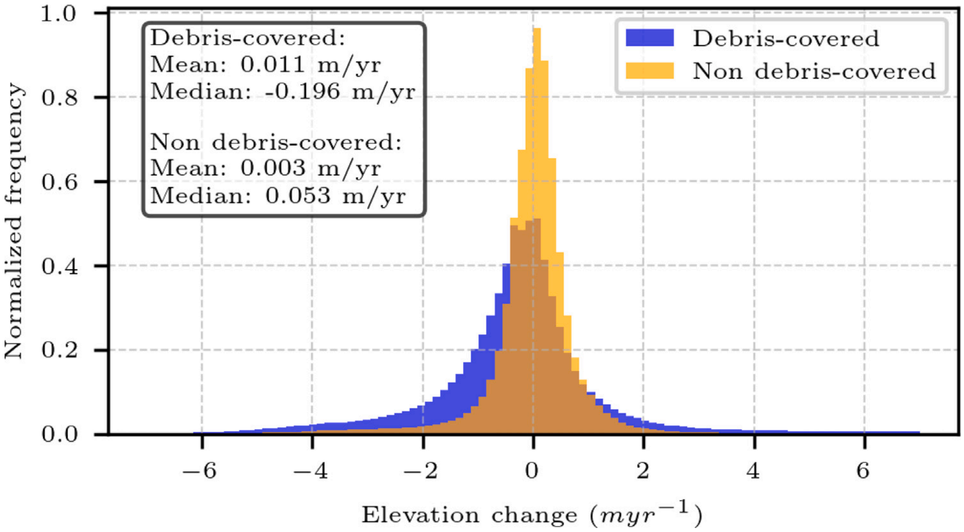

Fig. 16. Distribution of glacier elevation change rates (dh/dt) for debris-covered and non debris-covered areas. The histogram illustrates the normalized frequency of dh/dt values.

order of magnitude lower than those reported in related studies (Fig. 13), primarily due to the high vertical accuracy of the TanDEM-X DEMs generated through our iterative refinement method.

To verify the quality of our DEMs generation approach, we conducted extensive validation of the 2019 DEM mosaic using ICESat −2 data, which demonstrated an overall vertical error of 3.53 m (Fig. 10). Assuming similar vertical accuracy for the 2011 DEM mosaic, the theoretical vertical accuracy of the differential DEM (dDEM) between these two mosaics would be approximately 2.49 m, or 0.31 m yr^{-1} when normalized by time. This theoretical estimate closely aligns with our empirical proxy uncertainty measurement of 0.20 m yr^{-1} observed on stable ground, confirming the reliability of our methodology.

When placed in the context of existing literature, the significance of our improved accuracy becomes apparent. Previous studies have typically reported much higher uncertainty values for dh/dt over stable ground, generally around 1–2 m yr^{-1}. For instance, Berthier and Brun (2019) measured an uncertainty of 1.12 m yr^{-1} on stable ground using ASTER DEM, resulting in a mass balance uncertainty of ±0.15 m w.e.yr^{-1}. Similarly, Rankl and Braun (2016) reported an uncertainty of 1.90 m yr^{-1} for elevation differences between TanDEM-X and SRTM-X DEMs, yielding an uncertainty of ±0.12 m yr^{-1} for mean glacier elevation change. Lv et al. (2020) documented vertical uncertainties ranging from 5–10 m over stable ground for a time span of approximately 5 years, with an uncertainty of ±0.04 m yr^{-1} for the mean mass balance of 55 glaciers in eastern Pamir. Compared to these studies, the vertical uncertainty of dh/dt in our work is significantly lower by an order of magnitude, resulting in substantially reduced uncertainty in both glacier mean elevation change and mass balance estimations.

The improvement in uncertainty quantification can be attributed primarily to our methodological choices. The exceptionally low uncertainty in our results underscored the value of TanDEM-X DEMs for glacier mass balance estimation. The TanDEM-X 2020 mission phase provided a unique opportunity to generate high-resolution DEM pairs over extended time spans (exceeding 5 years), which is ideal for precise glacier mass balance calculations. Furthermore, by exclusively using DEMs generated from SAR data, the proposed method can substantially reduce the penetration bias typically caused by different sensors and acquisition modes (Dehecq et al., 2016; Rignot et al., 2001; Abdullah et al., 2020).

Beyond DEM generation, the voids filling approach also contributed to uncertainty reduction. In this work, the challenge of dDEM void filling was addressed using the GPR method, which enabled both the reconstruction of spatial patterns in dDEM voids and the estimation of uncertainty across filled areas. Notably, the void uncertainty proved independent of measurement coverage and GPR model training performance, indicating robust and effective inference of missing values in the dDEM. By properly propagating void uncertainty into the total uncertainty calculation, this approach enabled reliable mass balance estimation considering both measurement and voids filling errors. Future work could involve a systematic comparison of the GPR approach with other gap-filling methods, such as linear and hypsometric interpolation (McNabb et al., 2019), to further validate its effectiveness and identify optimal strategies for different glacier conditions.

6. Conclusion

In this study, we measured elevation changes and mass balances across 681 glaciers in the Karakoram region, covering over 10,000 km^2 of glaciated area. The results indicated a slightly negative or near-equilibrium status for the region, but with strong spatial heterogeneity in glacier dynamics and mass balances. The regional mean dh/dt was 0.0038 ± 0.0042 m yr^{-1}, and the regional specific mass balance was 0.0032 ± 0.0052 m w.e. yr^{-1}. These values are consistent with previous studies reporting near-stable conditions for the Karakoram glaciers. Within the region, surge-type glaciers exhibited distinct behaviors, with an average dh/dt of 0.019 ± 0.0052 m yr^{-1} and a specific mass balance of 0.0161 ± 0.0063 m w.e. yr^{-1}. In contrast, non-surge glaciers showed an average dh/dt of -0.0058 ± 0.0044 m yr^{-1} and a specific mass balance of -0.049 ± 0.0067 m w.e. yr^{-1}. Spatial patterns revealed increasing thickening from east to west, except for a cluster of debris-covered glaciers in the western part of the region. Overall, the findings suggest a slight thinning trend for Karakoram glaciers during the study period, highlighting the complex and heterogeneous glacier behavior in the region.

The detailed elevation and mass change measurement were enabled by the comprehensive framework proposed in this work, which integrated three core modules to overcome the challenges of glacier mass balance assessments in complex mountainous terrains. The first module involves the generation of high-resolution, high-accuracy DEMs using individual TanDEM-X interferometric acquisitions, leveraging the TanDEM-X 2020 mission phase to enable long time-span measurements for the mass balance. The second module processed dDEM mosaics to produce time-sensitive, void-free dh/dt maps. The use of the GPR modeling approach for void filling ensured that uncertainties in data gaps are properly quantified. The third module incorporated rigorous uncertainty propagation methods, ensuring properly quantified uncertainties by modeling heteroskedasticity and spatial error correlations. By integrating these modules, the framework provided a robust and scalable solution for producing accurate elevation change and mass balance measurements, even in highly heterogeneous and data-sparse regions.

In summary, this study advanced the understanding of glacier dynamics in the Karakoram region and addressed the challenges of measuring mass balance in its complex mountainous terrain. Beyond the measurement results, the proposed framework provided a scalable and adaptable solution for future studies in other glaciated regions. By integrating high-resolution DEM generation, advanced dDEM processing, and robust uncertainty quantification, the proposed framework enhanced the accuracy and reliability of glacier mass balance assessments. These contributions not only improve our understanding of glacier responses to climate change but also establish a methodological foundation for studying regional glacier behavior globally.

CRediT authorship contribution statement

Shiyi Li: Writing – review & editing, Writing – original draft, Visualization, Validation, Methodology, Formal analysis, Data curation, Conceptualization. **Irena Hajnsek:** Writing – review & editing, Supervision, Project administration, Conceptualization.

Declaration of Generative AI and AI-assisted technologies in the writing process

During the preparation of this work the lead author S. Li used ChatGPT in order to improve clarity and language use of the manuscript. After using this tool on targeted sentences, the author reviewed and edited the content as needed and takes full responsibility for the content of the publication.

Declaration of competing interest

The authors declare that they have no known competing financial interests or personal relationships that could have appeared to influence the work reported in this paper.

Acknowledgments

The authors would like to thank Dr. Silvan Leinss, Dr. Lanqing Huang and Dr. Philipp Bernhard for their valuable advice during the development of the method. The TanDEM-X data used in this article was provided by the German Space Agency (DLR) via proposal XTI_GEOL7437.

Appendix A. Proof of regional mass balance uncertainty propagation

The area-weighted average dh/dt for the entire region can be calculated as:

$$\overline{dh}_{\Sigma} = \frac{\sum_{i=1}^{N} A_i \cdot \overline{dh}_i}{\sum_{i=1}^{N} A_i}, \tag{A.1}$$

where A_i is the area of the ith glacier, $\overline{dh}_i$ is the average dh/dt of the ith glacier, and N is the total number of glaciers in the region. To estimate the uncertainty of $\overline{dh}_{\Sigma}$, we apply the first-order Taylor expansion for both A_i and $\overline{dh}_i$, assuming independence between the two variables and independence for errors of A_i between glaciers, to obtain:

$$\sigma^2_{\overline{dh}_{\Sigma}} = \sum_{i}^{N}\left[\left(\frac{\partial \overline{dh}_{\Sigma}}{\partial A_i}\right)^2 \sigma^2_{A_i} + \left(\frac{\partial \overline{dh}_{\Sigma}}{\partial \overline{dh}_i}\right)^2 \sigma^2_{\overline{dh}_i}\right] + 2\sum_{i<j} \frac{\partial \overline{dh}_{\Sigma}}{\partial \overline{dh}_i}\frac{\partial \overline{dh}_{\Sigma}}{\partial \overline{dh}_j}\mathrm{Cov}(\overline{dh}_i, \overline{dh}_j)$$

where σ_{A_i} and $\sigma_{\overline{dh}_i}$ are the uncertainties of A_i and $\overline{dh}_i$, respectively, and $\mathrm{Cov}(\overline{dh}_i, \overline{dh}_j)$ is the covariance between $\overline{dh}_i$ and $\overline{dh}_j$. The covariance term is zero if the errors of $\overline{dh}_i$ are independent between glaciers, however it must be considered in our case due to the spatial correlation of the errors.

Let $T = \sum A_i$, the partial derivatives of $\overline{dh}_{\Sigma}$ with respect to A_i and $\overline{dh}_i$ can be derived as:

$$\frac{\partial \overline{dh}_{\Sigma}}{\partial A_i} = \frac{\overline{dh}_i T - \sum A_i \overline{dh}_i}{T^2} = \frac{\overline{dh}_i - \overline{dh}_{\Sigma}}{T},$$

$$\frac{\partial \overline{dh}_{\Sigma}}{\partial \overline{dh}_i} = \frac{A_i}{T}$$

which can be substituted into the equation above to obtain the uncertainty of $\overline{dh}_{\Sigma}$ as:

$$\sigma^2_{\overline{dh}_{\Sigma}} = \frac{1}{T^2}\left[\sum_{i}^{N}\left(\overline{dh}_i - \overline{dh}_{\Sigma}\right)^2 \sigma^2_{A_i} + \sum_{i}^{N} A_i^2 \sigma^2_{\overline{dh}_i} + \sum_{i\neq j}^{N} A_i A_j \mathrm{Cov}(\overline{dh}_i, \overline{dh}_j)\right] \tag{A.2}$$

Converting the summation to a double summation over all pairs of glaciers, we have:

$$\sigma^2_{\overline{dh}_{\Sigma}} = \frac{1}{T^2}\left[\sum_{i}^{N}\left(\overline{dh}_i - \overline{dh}_{\Sigma}\right)^2 \sigma^2_{A_i} + \sum_{i}^{N}\sum_{j}^{N} A_i A_j \mathrm{Cov}(\overline{dh}_i, \overline{dh}_j)\right] \tag{A.3}$$

Consider variogram

$$V = V(\sigma_{\overline{dh}_i}, \sigma_{\overline{dh}_j}, r, d)$$

where r is the correlation range and d is the distance between glacier i and j. Assuming second-order stationarity, the covariance term can be expressed as:

$$\mathrm{Cov}(\overline{dh}_i, \overline{dh}_j) = \sigma_{\overline{dh}_i}\sigma_{\overline{dh}_j} - V(\sigma_{\overline{dh}_i}, \sigma_{\overline{dh}_j}, r, d) \tag{A.4}$$

replacing the covariance term in Eq. (A.3), and re-write the summation as a double summation over all pairs of glaciers, we have:

$$\sigma^2_{\overline{dh}_{\Sigma}} = \frac{1}{T^2}\left[\sum_{i}^{N}\left(\overline{dh}_i - \overline{dh}_{\Sigma}\right)^2 \sigma^2_{A_i} + \sum_{i}^{N}\sum_{j}^{N} A_i A_j \left(\sigma_{\overline{dh}_i}\sigma_{\overline{dh}_j} - V\right)\right] \tag{A.5}$$

In Eq. (A.5), the first term shows that the uncertainty of glacier area is scaled by the deviation of the glacier's average $\overline{dh}$ from the regional weighted average $\overline{dh}_{\Sigma}$. The second term shows that the uncertainty of the regional weighted average, adjusted by the correlation between glaciers, is scaled by the product of the glacier areas. Note that the second term

$$\frac{1}{T^2}\sum_{i}^{N}\sum_{j}^{N} A_i A_j (\sigma_{\overline{dh}_i}\sigma_{\overline{dh}_j} - V)$$

is the same as the uncertainty propagation of spatial ensembles derived by Hugonnet et al. (2022).

Data availability

Data will be made available on request.

References

Abdullah, T., Romshoo, S.A., Rashid, I., 2020. The satellite observed glacier mass changes over the Upper Indus Basin during 2000–2012. Sci. Rep. 10 (1), 14285. http://dx.doi.org/10.1038/s41598-020-71281-7.

Abdullahi, S., Wessel, B., Huber, M., Wendleder, A., Roth, A., Kuenzer, C., 2019. Estimating penetration-related X-band InSAR elevation bias: A study over the greenland ice sheet. Remote. Sens. 11 (24), 2903. http://dx.doi.org/10.3390/rs11242903, URL: https://www.mdpi.com/2072-4292/11/24/2903.

Agarwal, V., Bolch, T., Syed, T.H., Pieczonka, T., Strozzi, T., Nagaich, R., 2017. Area and mass changes of Siachen glacier (East Karakoram). J. Glaciol. 63 (237), 148–163. http://dx.doi.org/10.1017/jog.2016.127, URL: https://www.cambridge.org/core/journals/journal-of-glaciology/article/area-and-mass-changes-of-siachen-glacier-east-karakoram/65D24065F5F1E0965E2BA4F1F8B312DE.

Azam, M.F., Wagnon, P., Berthier, E., Vincent, C., Fujita, K., Kargel, J.S., 2018. Review of the status and mass changes of Himalayan-Karakoram glaciers. J. Glaciol. 64 (243), 61–74. http://dx.doi.org/10.1017/jog.2017.86, URL: https://www.cambridge.org/core/journals/journal-of-glaciology/article/review-of-the-status-and-mass-changes-of-himalayankarakoram-glaciers/BDF72DED08FC3BC6584CD4F745EB1595.

Berthier, E., Brun, F., 2019. Karakoram geodetic glacier mass balances between 2008 and 2016: persistence of the anomaly and influence of a large rock avalanche on Siachen Glacier. J. Glaciol. 65 (251), 494–507. http://dx.doi.org/10.1017/jog.2019.32, URL: https://www.cambridge.org/core/journals/journal-of-glaciology/article/karakoram-geodetic-glacier-mass-balances-between-2008-and-2016-persistence-of-the-anomaly-and-influence-of-a-large-rock-avalanche-on-siachen-glacier/131C4EF02593AA45D0119A80668BEEC7.

Bhambri, R., Bolch, T., Kawishwar, P., Dobhal, D.P., Srivastava, D., Pratap, B., 2013. Heterogeneity in glacier response in the upper Shyok valley, northeast Karakoram. Cryosphere 7 (5), 1385–1398. http://dx.doi.org/10.5194/tc-7-1385-2013, URL: https://tc.copernicus.org/articles/7/1385/2013/.

Bolibar, J., Rabatel, A., Gouttevin, I., Zekollari, H., Galiez, C., 2022. Nonlinear sensitivity of glacier mass balance to future climate change unveiled by deep learning. Nat. Commun. 13 (1), 409. http://dx.doi.org/10.1038/s41467-022-28033-0, URL: https://www.nature.com/articles/s41467-022-28033-0.

Brun, F., Berthier, E., Wagnon, P., Kääb, A., Treichler, D., 2017. A spatially resolved estimate of high mountain Asia glacier mass balances from 2000 to 2016. Nat. Geosci. 10 (9), 668–673. http://dx.doi.org/10.1038/ngeo2999, URL: https://www.nature.com/articles/ngeo2999.

Cogley, J.G., 2009. Geodetic and direct mass-balance measurements: Comparison and joint analysis. Ann. Glaciol. 50 (50), 96–100. http://dx.doi.org/10.3189/172756409787769744, URL: https://www.cambridge.org/core/journals/annals-of-glaciology/article/geodetic-and-direct-massbalance-measurements-comparison-and-joint-analysis/56652FA8B1A73794947DCAB7B0D53870.

Copland, L., Sylvestre, T., Bishop, M.P., Shroder, J.F., Seong, Y.B., Owen, L.A., Bush, A., Kamp, U., 2011. Expanded and recently increased glacier surging in the Karakoram. Arct. Antarct. Alp. Res. 43 (4), 503–516. http://dx.doi.org/10.1657/1938-4246-43.4.503, URL: https://bioone.org/journals/Arctic-Antarctic-and-Alpine-Research/volume-43/issue-4/1938-4246-43.4.503/Expanded-and-Recently-Increased-Glacier-Surging-in-the-Karakoram/10.1657/1938-4246-43.4.503.full.

Dehecq, A., Millan, R., Berthier, E., Gourmelen, N., Trouvé, E., Vionnet, V., 2016. Elevation changes inferred from TanDEM-X data over the mont-blanc area: Impact of the X-band interferometric bias. IEEE J. Sel. Top. Appl. Earth Obs. Remote. Sens. 9 (8), 3870–3882. http://dx.doi.org/10.1109/JSTARS.2016.2581482, URL: https://ieeexplore.ieee.org/document/7518587.

Dimri, A.P., 2021. Decoding the Karakoram anomaly. Sci. Total Environ. 788, 147864. http://dx.doi.org/10.1016/j.scitotenv.2021.147864, URL: https://www.sciencedirect.com/science/article/pii/S0048969721029351.

Dowd, P.A., 1984. The Variogram and kriging: Robust and resistant estimators. In: Verly, G., David, M., Journel, A.G., Marechal, A. (Eds.), Geostatistics for Natural Resources Characterization: Part 1. Springer Netherlands, Dordrecht, pp. 91–106. http://dx.doi.org/10.1007/978-94-009-3699-7_6.

Dussaillant, I., Hugonnet, R., Huss, M., Berthier, E., Bannwart, J., Paul, F., Zemp, M., 2024. Annual mass changes for each glacier in the world from 1976 to 2023. Earth Syst. Sci. Data Discuss. 1–41. http://dx.doi.org/10.5194/essd-2024-323, URL: https://essd.copernicus.org/preprints/essd-2024-323/.

European Space Agency, Airbus, 2022. Copernicus DEM. http://dx.doi.org/10.5270/ESA-c5d3d65, URL: https://spacedata.copernicus.eu/collections/copernicus-digital-elevation-model.

Farinotti, D., 2013. On the effect of short-term climate variability on mountain glaciers: insights from a case study. J. Glaciol. 59 (217), 992–1006. http://dx.doi.org/10.3189/2013JoG13J080, URL: https://www.cambridge.org/core/journals/journal-of-glaciology/article/on-the-effect-of-shortterm-climate-variability-on-mountain-glaciers-insights-from-a-case-study/AC4DD47E48AC2723604A1B7C4AB1C272.

Farinotti, D., Immerzeel, W.W., Kok, R.J.d., Quincey, D.J., Dehecq, A., 2020. Manifestations and mechanisms of the Karakoram glacier anomaly. Nat. Geosci. 13 (1), 8–16. http://dx.doi.org/10.1038/s41561-019-0513-5, URL: https://www.nature.com/articles/s41561-019-0513-5.

Gardelle, J., Berthier, E., Arnaud, Y., 2012. Slight mass gain of Karakoram glaciers in the early twenty-first century. Nat. Geosci. 5 (5), 322–325. http://dx.doi.org/10.1038/ngeo1450, URL: https://www.nature.com/articles/ngeo1450.

Gardelle, J., Berthier, E., Arnaud, Y., Kääb, A., 2013-08-09. Region-wide glacier mass balances over the Pamir-Karakoram-Himalaya during 1999–2011. Cryosphere 7 (4), 1263–1286. http://dx.doi.org/10.5194/tc-7-1263-2013, URL: https://tc.copernicus.org/articles/7/1263/2013/.

Gardner, J.R., Pleiss, G., Bindel, D., Weinberger, K.Q., Wilson, A.G., 2021. GPyTorch: Blackbox matrix-matrix Gaussian process inference with GPU acceleration. http://dx.doi.org/10.48550/arXiv.1809.11165, URL: http://arxiv.org/abs/1809.11165.

Guo, L., Li, J., Li, Z.-w., Wu, L.-x., Li, X., Hu, J., Li, H.-l., Li, H.-y., Miao, Z.-l., Li, Z.-q., 2020. The surge of the hispar glacier, central Karakoram: SAR 3-D flow velocity time series and thickness changes. J. Geophys. Res.: Solid Earth 125 (7), e2019JB018945. http://dx.doi.org/10.1029/2019JB018945, URL: https://onlinelibrary.wiley.com/doi/abs/10.1029/2019JB018945.

Hajnsek, I., Busche, T., Abdullahi, S., Bachmann, M., Baumgartner, S.V., Bojarski, A., Bueso-Bello, J.-L., Esch, T., Fritz, T., Alonso-Gonzalez, A., Gonzalez, C., Huang, L., Kraus, T., Lachaise, M., Li, S., Dekker, F.L., Maier, K., Martone, M., Milillo, P., Mittermayer, J., Nannini, M., Papathanassiou, K., Pardini, M., Pinheiro, M., Prats-Iraola, P., Rizzoli, P., Rodriguez-Cassola, M., Roth, A., Schandri, M., Scheiber, R., Steinbrecher, U., Schweisshelm, B., Villano, M., Warmedinger, L.J., Wessel, B., Krieger, G., Zink, M., Moreira, A., 2025. TanDEM-X: The 4D mission phase for earth surface dynamics: Science activities highlights and new data products after 15 years of bistatic operations. IEEE Geosci. Remote. Sens. Mag. 2–37. http://dx.doi.org/10.1109/MGRS.2024.3525403, URL: https://ieeexplore.ieee.org/document/10925374/?arnumber=10925374&tag=1.

Herreid, S., Pellicciotti, F., 2020-09-02. The state of rock debris covering Earth's glaciers. Nat. Geosci. 13 (9), 621–627. http://dx.doi.org/10.1038/s41561-020-0615-0, URL: https://www.nature.com/articles/s41561-020-0615-0.

Hewitt, K., 2005. The karakoram anomaly? Glacier expansion and the 'Elevation Effect,' karakoram himalaya. Mt. Res. Dev. 25 (4), 332–340. http://dx.doi.org/10.1659/0276-4741(2005)025[0332:TKAGEA]2.0.CO;2, URL: https://bioone.org/journals/mountain-research-and-development/volume-25/issue-4/0276-4741_2005_025_0332_TKAGEA_2.0.CO_2/The-Karakoram-Anomaly-Glacier-Expansion-and-the-Elevation-Effect-Karakoram/10.1659/0276-4741(2005)025[0332:TKAGEA]2.0.CO;2.full.

Hewitt, K., 2014. Glaciers of the Karakoram himalaya: Glacial environments, processes, hazards and resources. In: Advances in Asian Human-Environmental Research, Springer Netherlands, Dordrecht, http://dx.doi.org/10.1007/978-94-007-6311-1, URL: https://link.springer.com/10.1007/978-94-007-6311-1.

Hirabayashi, Y., Döll, P., Kanae, S., 2010. Global-scale modeling of glacier mass balances for water resources assessments: Glacier mass changes between 1948 and 2006. J. Hydrol. 390 (3–4), 245–256. http://dx.doi.org/10.1016/j.jhydrol.2010.07.001, URL: https://linkinghub.elsevier.com/retrieve/pii/S0022169410004142.

Hugonnet, R., Brun, F., Berthier, E., Dehecq, A., Mannerfelt, E.S., Eckert, N., Farinotti, D., 2022. Uncertainty analysis of digital elevation models by spatial inference from stable terrain. IEEE J. Sel. Top. Appl. Earth Obs. Remote. Sens. 15, 6456–6472. http://dx.doi.org/10.1109/JSTARS.2022.3188922, URL: https://ieeexplore.ieee.org/document/9815885.

Hugonnet, R., McNabb, R., Berthier, E., Menounos, B., Nuth, C., Girod, L., Farinotti, D., Huss, M., Dussaillant, I., Brun, F., Kääb, A., 2021. Accelerated global glacier mass loss in the early twenty-first century. Nature 592 (7856), 726–731. http://dx.doi.org/10.1038/s41586-021-03436-z, URL: https://www.nature.com/articles/s41586-021-03436-z.

Huo, D., Bishop, M.P., Bush, A.B.G., 2021. Understanding complex debris-covered glaciers: Concepts, issues, and research directions. Front. Earth Sci. 9, 652279. http://dx.doi.org/10.3389/feart.2021.652279, URL: https://www.frontiersin.org/articles/10.3389/feart.2021.652279/full.

Huss, M., 2013. Density assumptions for converting geodetic glacier volume change to mass change. Cryosphere 7 (3), 877–887. http://dx.doi.org/10.5194/tc-7-877-2013, URL: https://tc.copernicus.org/articles/7/877/2013/.

Huss, M., Hock, R., 2018. Global-scale hydrological response to future glacier mass loss. Nat. Clim. Chang. 8 (2), 135–140. http://dx.doi.org/10.1038/s41558-017-0049-x, URL: https://www.nature.com/articles/s41558-017-0049-x.

IPCC, 2022. The Ocean and Cryosphere in a Changing Climate: Special Report of the Intergovernmental Panel on Climate Change. Cambridge University Press, Cambridge, http://dx.doi.org/10.1017/9781009157964, URL: https://www.cambridge.org/core/books/ocean-and-cryosphere-in-a-changing-climate/A05E6C9F8638FA7CE1748DE2EB7B491B.

Jiang, Z., Wu, K., Liu, S., Wang, X., Zhang, Y., Tahir, A.A., Long, S., 2021. Surging dynamics of South Rimo Glacier, Eastern Karakoram. Environ. Res. Lett. 16 (11), 114044. http://dx.doi.org/10.1088/1748-9326/ac3175.

Kääb, A., Berthier, E., Nuth, C., Gardelle, J., Arnaud, Y., 2012. Contrasting patterns of early twenty-first-century glacier mass change in the Himalayas. Nature 488 (7412), 495–498. http://dx.doi.org/10.1038/nature11324, URL: https://www.nature.com/articles/nature11324.

Kääb, A., Treichler, D., Nuth, C., Berthier, E., 2015. Brief communication: Contending estimates of 2003–2008 glacier mass balance over the Pamir–Karakoram–Himalaya. Cryosphere 9 (2), 557–564. http://dx.doi.org/10.5194/tc-9-557-2015, URL: https://tc.copernicus.org/articles/9/557/2015/.

Kapnick, S.B., Delworth, T.L., Ashfaq, M., Malyshev, S., Milly, P.C.D., 2014. Snowfall less sensitive to warming in Karakoram than in Himalayas due to a unique seasonal cycle. Nat. Geosci. 7 (11), 834–840. http://dx.doi.org/10.1038/ngeo2269, URL: https://www.nature.com/articles/ngeo2269.

Krieger, G., Zink, M., Bachmann, M., Bräutigam, B., Schulze, D., Martone, M., Rizzoli, P., Steinbrecher, U., Walter Antony, J., De Zan, F., Hajnsek, I., Papathanassiou, K., Kugler, F., Rodriguez Cassola, M., Younis, M., Baumgartner, S., López-Dekker, P., Prats, P., Moreira, A., 2013. TanDEM-X: A radar interferometer with two formation-flying satellites. Acta Astronaut. 89, 83–98. http://dx.doi.org/10.1016/j.actaastro.2013.03.008, URL: https://www.sciencedirect.com/science/article/pii/S0094576513000805.

Lachaise, M., Schweisshelm, B., Fritz, T., 2020. The new tandem-X change dem: Specifications and interferometric processing. In: 2020 IEEE Latin American GRSS & ISPRS Remote Sensing Conference. LAGIRS, IEEE, Santiago, Chile, pp. 646–651. http://dx.doi.org/10.1109/LAGIRS48042.2020.9165638, URL: https://ieeexplore.ieee.org/document/9165638/.

Leinss, S., Bernhard, P., 2021. TanDEM-X:Deriving InSAR height changes and velocity dynamics of great aletsch glacier. IEEE J. Sel. Top. Appl. Earth Obs. Remote. Sens. 14, 4798–4815. http://dx.doi.org/10.1109/JSTARS.2021.3078084.

Lhakpa, D., Fan, Y., Cai, Y., 2022. Continuous Karakoram Glacier anomaly and its response to climate change during 2000–2021. Remote. Sens. 14 (24), 6281. http://dx.doi.org/10.3390/rs14246281, URL: https://www.mdpi.com/2072-4292/14/24/6281.

Li, S., Leinss, S., Bernhard, P., Hajnsek, I., 2021. Recent surge of the South Rimo Glacier, Karakoram: Dynamics characterization using SAR data. In: 2021 IEEE International Geoscience and Remote Sensing Symposium IGARSS. pp. 5520–5523. http://dx.doi.org/10.1109/IGARSS47720.2021.9553193.

Li, J., Sun, M., Yao, X., Duan, H., Zhang, C., Wang, S., Niu, S., Yan, X., 2023. A review of Karakoram glacier anomalies in high mountains Asia. Water 15 (18), 3215. http://dx.doi.org/10.3390/w15183215, URL: https://www.mdpi.com/2073-4441/15/18/3215.

Lin, H., Li, G., Cuo, L., Hooper, A., Ye, Q., 2017. A decreasing glacier mass balance gradient from the edge of the Upper Tarim Basin to the Karakoram during 2000–2014. Sci. Rep. 7 (1), 6712. http://dx.doi.org/10.1038/s41598-017-07133-8, URL: https://www.nature.com/articles/s41598-017-07133-8.

Liu, X., Xu, Z., Yang, H., Vaghefi, S.A., 2021. Responses of the glacier mass balance to climate change in the Tibetan plateau during 1975–2013. J. Geophys. Res.: Atmospheres 126 (7), e2019JD032132. http://dx.doi.org/10.1029/2019JD032132, URL: https://onlinelibrary.wiley.com/doi/abs/10.1029/2019JD032132.

Lv, M., Quincey, D.J., Guo, H., King, O., Liu, G., Yan, S., Lu, X., Ruan, Z., 2020. Examining geodetic glacier mass balance in the eastern Pamir transition zone. J. Glaciol. 66 (260), 927–937. http://dx.doi.org/10.1017/jog.2020.54, URL: https://www.cambridge.org/core/journals/journal-of-glaciology/article/examining-geodetic-glacier-mass-balance-in-the-eastern-pamir-transition-zone/B1F6F73B08E44FD36615902B3DDF34B9.

Mayer, C., Licciulli, C., 2021. The concept of steady state, cyclicity and debris unloading of debris-covered glaciers. Front. Earth Sci. 9, 710276. http://dx.doi.org/10.3389/feart.2021.710276, URL: https://www.frontiersin.org/articles/10.3389/feart.2021.710276/full.

McNabb, R., Nuth, C., Kääb, A., Girod, L., 2019. Sensitivity of glacier volume change estimation to DEM void interpolation. Cryosphere 13 (3), 895–910. http://dx.doi.org/10.5194/tc-13-895-2019, URL: https://tc.copernicus.org/articles/13/895/2019/.

Miles, K.E., Hubbard, B., Quincey, D.J., Miles, E.S., Sherpa, T.C., Rowan, A.V., Doyle, S.H., 2018. Polythermal structure of a Himalayan debris-covered glacier revealed by borehole thermometry. Sci. Rep. 8 (1), 16825. http://dx.doi.org/10.1038/s41598-018-34327-5, URL: https://www.nature.com/articles/s41598-018-34327-5.

Millan, R., Dehecq, A., Trouvé, E., Gourmelen, N., Berthier, E., 2015. Elevation changes and X-band ice and snow penetration inferred from TanDEM-X data of the Mont-Blanc area. In: 2015 8th International Workshop on the Analysis of Multitemporal Remote Sensing Images (Multi-Temp). pp. 1–4. http://dx.doi.org/10.1109/Multi-Temp.2015.7245753, URL: https://ieeexplore.ieee.org/abstract/document/7245753.

Mukhopadhyay, B., Khan, A., 2014. Rising river flows and glacial mass balance in central Karakoram. J. Hydrol. 513, 192–203. http://dx.doi.org/10.1016/j.jhydrol.2014.03.042, URL: https://www.sciencedirect.com/science/article/pii/S0022169414002273.

Nie, Y., Pritchard, H.D., Liu, Q., Hennig, T., Wang, W., Wang, X., Liu, S., Nepal, S., Samyn, D., Hewitt, K., Chen, X., 2021. Glacial change and hydrological implications in the Himalaya and Karakoram. Nat. Rev. Earth & Environ. 2 (2), 91–106. http://dx.doi.org/10.1038/s43017-020-00124-w, URL: https://www.nature.com/articles/s43017-020-00124-w.

Nuth, C., Kääb, A., 2011. Co-registration and bias corrections of satellite elevation data sets for quantifying glacier thickness change. Cryosphere 5 (1), 271–290. http://dx.doi.org/10.5194/tc-5-271-2011, URL: https://tc.copernicus.org/articles/5/271/2011/tc-5-271-2011.html.

Piermattei, L., Zemp, M., Sommer, C., Brun, F., Braun, M.H., Andreassen, L.M., Belart, J.M.C., Berthier, E., Bhattacharya, A., Boehm Vock, L., Bolch, T., Dehecq, A., Dussaillant, I., Falaschi, D., Florentine, C., Floricioiu, D., Ginzler, C., Guillet, G., Hugonnet, R., Huss, M., Kääb, A., King, O., Klug, C., Knuth, F., Krieger, L., La Frenierre, J., McNabb, R., McNeil, C., Prinz, R., Sass, L., Seehaus, T., Shean, D., Treichler, D., Wendt, A., Yang, R., 2024. Observing glacier elevation changes from spaceborne optical and radar sensors – an inter-comparison experiment using ASTER and TanDEM-X data. Cryosphere 18 (7), 3195–3230. http://dx.doi.org/10.5194/tc-18-3195-2024, URL: https://tc.copernicus.org/articles/18/3195/2024/.

Quincey, D.J., Braun, M., Glasser, N.F., Bishop, M.P., Hewitt, K., Luckman, A., 2011. Karakoram glacier surge dynamics. Geophys. Res. Lett. 38 (18), http://dx.doi.org/10.1029/2011GL049004, URL: https://agupubs.onlinelibrary.wiley.com/doi/abs/10.1029/2011GL049004.

Quincey, D.J., Glasser, N.F., Cook, S.J., Luckman, A., 2015. Heterogeneity in Karakoram glacier surges: KARAKORAM GLACIER SURGE HETEROGENEITY. J. Geophys. Res.: Earth Surf. 120 (7), 1288–1300. http://dx.doi.org/10.1002/2015JF003515, URL: http://doi.wiley.com/10.1002/2015JF003515.

Radić, V., Hock, R., 2014. Glaciers in the earth's hydrological cycle: Assessments of glacier mass and runoff changes on global and regional scales. Surv. Geophys. 35 (3), 813–837. http://dx.doi.org/10.1007/s10712-013-9262-y, URL: http://link.springer.com/10.1007/s10712-013-9262-y.

Ragettli, S., Bolch, T., Pellicciotti, F., 2016-09-14. Heterogeneous glacier thinning patterns over the last 40 years in Langtang Himal, Nepal. Cryosphere 10 (5), 2075–2097. http://dx.doi.org/10.5194/tc-10-2075-2016, URL: https://tc.copernicus.org/articles/10/2075/2016/.

Rankl, M., Braun, M., 2016. Glacier elevation and mass changes over the central Karakoram region estimated from TanDEM-X and SRTM/X-SAR digital elevation models. Ann. Glaciol. 57 (71), 273–281. http://dx.doi.org/10.3189/2016AoG71A024, URL: https://www.cambridge.org/core/product/identifier/S0260305500000288/type/journal_article.

RGI Consortium, 2023. Randolph Glacier Inventory - A Dataset of Global Glacier Outlines, Version 7. NASA National Snow and Ice Data Center Distributed Active Archive Center, http://dx.doi.org/10.5067/F6JMOVY5NAVZ, URL: https://nsidc.org/data/nsidc-0770/versions/7.

Rignot, E., Echelmeyer, K., Krabill, W., 2001. Penetration depth of interferometric synthetic-aperture radar signals in snow and ice. Geophys. Res. Lett. 28 (18), 3501–3504. http://dx.doi.org/10.1029/2000GL012484, URL: https://onlinelibrary.wiley.com/doi/abs/10.1029/2000GL012484.

Scherler, D., Bookhagen, B., Strecker, M.R., 2011. Spatially variable response of Himalayan glaciers to climate change affected by debris cover. Nat. Geosci. 4 (3), 156–159. http://dx.doi.org/10.1038/ngeo1068, URL: https://www.nature.com/articles/ngeo1068.

Schweisshelm, B., Lachaise, M., 2022. Calibration of the Tandem-X craw DEMs for the Tandem-X DEM change maps generation. In: IGARSS 2022 - 2022 IEEE International Geoscience and Remote Sensing Symposium. pp. 291–294. http://dx.doi.org/10.1109/IGARSS46834.2022.9883204, URL: https://ieeexplore.ieee.org/document/9883204.

Thapa, A., Muhammad, S., 2020. Contemporary snow changes in the Karakoram region attributed to improved MODIS data between 2003 and 2018. Water 12 (10), 2681. http://dx.doi.org/10.3390/w12102681, URL: https://www.mdpi.com/2073-4441/12/10/2681.

Usman, M., Furuya, M., 2018. Interannual modulation of seasonal glacial velocity variations in the Eastern Karakoram detected by ALOS-1/2 data. J. Glaciol. 64 (245), 465–476. http://dx.doi.org/10.1017/jog.2018.39, URL: https://www.cambridge.org/core/journals/journal-of-glaciology/article/interannual-modulation-of-seasonal-glacial-velocity-variations-in-the-eastern-karakoram-detected-by-alos12-data/C474AC55A195408CC798500932160B33.

Williams, C., Rasmussen, C., 1995. Gaussian processes for regression. In: Advances in Neural Information Processing Systems, vol. 8, MIT Press, URL: https://proceedings.neurips.cc/paper/1995/hash/7cce53cf90577442771720a370c3c723-Abstract.html.

Zemp, M., Jakob, L., Dussaillant, I., Nussbaumer, S.U., Gourmelen, N., Dubber, S., A, G., Abdullahi, S., Andreassen, L.M., Berthier, E., Bhattacharya, A., Blazquez, A., Boehm Vock, L.F., Bolch, T., Box, J., Braun, M.H., Brun, F., Cicero, E., Colgan, W., Eckert, N., Farinotti, D., Florentine, C., Floricioiu, D., Gardner, A., Harig, C., Hassan, J., Hugonnet, R., Huss, M., Jóhannesson, T., Liang, C.-C.A., Ke, C.-Q., Khan, S.A., King, O., Kneib, M., Krieger, L., Maussion, F., Mattea, E., McNabb, R., Menounos, B., Miles, E., Moholdt, G., Nilsson, J., Pálsson, F., Pfeffer, J., Piermattei, L., Plummer, S., Richter, A., Sasgen, I., Schuster, L., Seehaus, T., Shen, X., Sommer, C., Sutterley, T., Treichler, D., Velicogna, I., Wouters, B., Zekollari, H., Zheng, W., The GlaMBIE Team, 2025. Community estimate of global glacier mass changes from 2000 to 2023. Nature 1–7. http://dx.doi.org/10.1038/s41586-024-08545-z, URL: https://www.nature.com/articles/s41586-024-08545-z.

Zemp, M., Thibert, E., Huss, M., Stumm, D., Rolstad Denby, C., Nuth, C., Nussbaumer, S.U., Moholdt, G., Mercer, A., Mayer, C., Joerg, P.C., Jansson, P., Hynek, B., Fischer, A., Escher-Vetter, H., Elvehøy, H., Andreassen, L.M., 2013. Reanalysing glacier mass balance measurement series. Cryosphere 7 (4), 1227–1245. http://dx.doi.org/10.5194/tc-7-1227-2013, URL: https://tc.copernicus.org/articles/7/1227/2013/.

Zhao, F., Long, D., Fang, C., Wang, Y., Duan, X., 2025. Satellite-observed surging dynamics of North Kunchhang Glacier I in the Eastern Karakoram. EGUsphere 1–36. http://dx.doi.org/10.5194/egusphere-2025-652, URL: https://egusphere.copernicus.org/preprints/2025/egusphere-2025-652/.

Zink, M., Bachmann, M., Brautigam, B., Fritz, T., Hajnsek, I., Moreira, A., Wessel, B., Krieger, G., 2014. TanDEM-X: The new global DEM takes shape. IEEE Geosci. Remote. Sens. Mag. 2 (2), 8–23. http://dx.doi.org/10.1109/MGRS.2014.2318895, URL: https://ieeexplore.ieee.org/abstract/document/6841793.